POLITECNICO DI TORINO

Collegio di Ingegneria Chimica e dei Materiali

Master of Science Course in Materials Engineering for Industry 4.0

Master of Science Thesis

Identification by inverse method and data analysis of mechanical behavior laws dedicated to the numerical simulation under machining conditions.



Tutors Candidate

Prof. Daniale UGUES
Prof. Frederic VALIORGUE
Dr. Renaud FERRIER

Oghenefegor Favour UGBINE

September 2025

Abstract

This research study develops and validates an inverse identification algorithm framework that couples Python automation with Abaqus finite-element simulations and a Levenberg-Marquardt (LM) optimiser to optimise the material behaviour parameters (Johnson-Cook (J-C) constitutive law and the Taylor-Quinney (T-Q) heat fraction) for orthogonal cutting of PH martensitic stainless steels. The algorithm loop perturbs parameters, builds finite-difference sensitivities, updates with LM, and rewrites the input automatically, resulting in four machining output conditions across five undeformed chip thicknesses of H_{ref} = 0.10-0.25millimetres (mm) for the chip thickness, tool-chip contact length, cutting force, and penetration force. In the absence of 15-5PH experimental machining data, validation was performed using 17-4PH numerical datasets with similar properties. The baseline (pre-optimised) simulation exhibits large residual error on average, 21.94% (chip thickness), 41.20% (contact length), 40.21% (cutting force), and 28.37% (penetration force), demonstrating that uncalibrated parameters are non-predictive for precision machining analysis. After optimisation, mean errors for the chip thickness, tool-chip contact length, cutting force, and penetration force were drastically reduced to 0.49%, 4.35%, 0.34%, and 0.14% respectively, with rapid, monotonic convergence of ≤5 iterations across all undeformed Chip Thickness (H_{refs}). Best and worst residual errors were 0.053% for the 0.10mm H_{ref} and 4.77% for the 0.25mm H_{ref} . The resulting single parameter set generalises from the 2D orthogonal configuration of different cut sections to a 3D validation, indicating readiness for predictive simulation that requires robust force and chip geometry, which is relevant for industrial purposes.

Acknowledgments

First and foremost, all glory and praise to God Almighty, whose divine guidance and boundless grace provided me with the strength, wisdom, and perseverance to complete this research study.

I am deeply grateful to my supervisors, Prof. Daniele Uges, Prof. Frederic Valiorgue, and Dr. Renaud Ferrier, for their valuable insight and steadfast mentorship throughout this research journey. Your insightful feedback was instrumental in shaping these research insights. My profound thanks go to my mother, Mrs. Emily Ugbine, for her unconditional love, endless sacrifices, and constant prayers. You are my foundation and my greatest source of inspiration.

I also extend my sincere appreciation to the Erasmus Mundus Programme Coordinator Prof. Cedric Courbon, Dr. Brayet Aurelie, and my local coordinator, Prof. Cedric Bosch for their exceptional coordination, guidance, and support of the programme. I wish to express my gratitude to all the professors who taught me during the course of my master's studies, most especially at the Politecnico di Torino. Your knowledge and dedication have been foundational to my academic development.

Furthermore, I extend my deepest appreciation to the European Commission for funding this journey. Thank you for deeming me worthy to be part of this master's degree program and for the incredible opportunity to study across three esteemed universities. My gratitude also goes to Misutech for the valuable opportunity and resources provided. Finally, to my colleagues and friends, thank you for the moments that made this experience memorable. This achievement is a testament to the support of you all.

Table of Contents

	Abstract		1
	Acknowle	edgments	II
	Table of (Contents	III
	List of Fig	gures	VI
	List of Ta	bles	VIII
	Nomencla	ature	IX
C	hapter 1	Introduction	1
	1.1. Back	ground of Machining	1
	1.2. Probl	em Statement	2
	1.3. Aims	and Objectives	3
	1.4. Indus	strial Relevance	4
C	hapter 2	Literature Review	6
	2.1. Defin	ition and Types of Machining (Orthogonal Cutting, Milling, Turning)	6
	2.1.1.	Severe Plastic Deformation Zones in Machining	6
	2.2. Mech	anical Behaviour Laws in Metal Cutting	10
	2.2.1.	The Johnson-Cook Constitutive Model	10
	2.2.2.	Friction and Taylor-Quinney Coefficient in Machining	12
	2.3. Expe	rimental Data in Machining: Chip Geometry, and Forces	14
	2.3.1.	Chip Thickness and Contact Length in Machining	15
	2.3.2.	Force Measurement in Machining	16
	2.4. Num	erical Simulation of Machining	21
2.5. Inverse Identification Methods			21
2.6. Gradient Sensitivity & Perturbation Techniques			23
	2.7. Resea	arch Gap	24

Chapter 3	Methodology	26
3.1. Overview of the Methodological Approach		26
3.2. Expe	rimental Approach	28
3.2.1.	Material Selection	29
3.2.2.	Cutting Parameters and Tool Geometry	29
3.3. Num	erical Simulation with Abaqus	31
3.3.1.	Uncut-Chip Thickness (<i>Href</i>) Computation	31
3.3.2.	Boundary Conditions and Friction	33
3.3.3.	Implementation of Johnson-Cook Parameters	35
3.4. Pytho	on-Abaqus Coupling	37
3.4.1.	ODB Data Extraction	37
3.4.2.	Automation Workflow	38
3.5. 2D ar	nd 3D Simulation Optimisation Workflow	43
3.5.1.	2D Calibration Stage (Orthogonal Cutting in Plane Strain)	43
3.5.2.	3D Validation Stage for the Full 3D Machining Simulation	44
Chapter 4	Results and Discussion	45
4.1. Comp	parison of Experimental and Simulated Results Across <i>Href</i> Cases	46
4.1.1.	Chip Thickness	47
4.1.2.	Contact Length	48
4.1.3.	Cutting Force (Tangential)	49
4.1.4.	Penetration Force (Thrust)	51
4.2. Resid	lual Error Analysis Before and After Optimization	53
4.2.1.	Baseline Model Errors (Pre-Optimization)	53
4.2.2.	Improved Model Errors (Optimization)	54
4.3. Conv	ergence Behaviour of the Optimization Algorithm	55
4.4. Analy	sis of Optimised Parameters and Physical Interpretation	57
45 Over	all Discussion and Implications	50

Chapter 5	Conclusion	61
5.1. Conclu	sion	61
5.2. Future	Work	62

List of Figures

Figure 1.1: Integrated Experimental–Numerical Workflow for Inverse Identifica	tion in		
Machining	4		
Figure 1.2 : Industrial Relevance of Inverse Identification Methodology	4		
Figure 2.1: Shear zones in orthogonal cutting [23]	8		
Figure 2.2 : Illustration of the different types of chips formed in machining [22].	9		
Figure 2.3: Model of heat partitioning at the tool-chip interface [29].	13		
Figure 2.4 : Geometry of orthogonal cutting [32].	16		
Figure 2.5 : Experimental setup for Cutting Force Measurement [33].			
Figure 2.6 : Cutting force measurement system [33].	18		
Figure 3.1: Python-Abaqus optimization framework, highlighting Experimen	tation,		
sensitivity analysis, and iterative updates.	27		
Figure 3.2: Workflow of the integrated experimental-numerical calibration pro-	rocess,		
from 2D FE modelling to 3D validation	28		
Figure 3.3 : Orthogonal Cutting Tools	30		
Figure 3.4 : Schematic of the orthogonal cutting model. (a) $3D$ view of a turning ope	eration		
and (b) the corresponding 2D plane strain cutting slice with uncut chip thickness	Href.		
[54]	32		
Figure 3.5: Schematic of a 2D finite element model, showing the cutting depth,	refine		
mesh and boundary conditions.	33		
Figure 3.6 : The inverse algorithm flowchart was adopted for the identification	of the		
material behaviour parameter on the Python interface.	38		
Figure 4.1: Numerical simulation results showing chip geometry, workpiece, and ${\sf t}$	ool for		
each <i>Href</i> case	46		
Figure 4.2 : Chip thickness against <i>Href</i> for both Experiment, Reference	e, and		
Optimisation.	48		
Figure 4.3 : Contact Length against Href for both Experiment, Reference	e, and		
Optimisation.	49		
Figure 4.4 : Cutting Force against Href for both Experiment, Reference	e, and		
Optimisation.	51		
Figure 4.5: Penetration Force against <i>Href</i> for both Experiment, Reference	e, and		
Ontimisation.	52		

Figure 4.6 : Error Convergence of Machining Output across all Href	56
Figure 4.7 : Error Convergence of Material Behaviour across all Href	58

List of Tables

Table 2.1 : Summary of Research Gaps and Thesis Contributions	25
Table 3.1: Johnson-Cook parameter and Heat Infraction for 17-4PH Stainless States	eel [51].
	29
Table 3.2 : Features of The Cutting Tools and their Parameters.	30
Table 3.3: Material Properties and Simulation Parameters for 15-5PH Stainle	ess Steel
Machining Model	34
Table 3.4: Johnson-Cook parameters and Taylor Quinney for 15-5 PH [39]	35
Table 3.5: Boundary Limit for the 15-5PH Stainless Steel.	42
Table 4.1: Percentage Error of Reference (Pre-Optimized) Model	53
Table 4.2: Percentage Error of Optimized Model	54
Table 4.3 : Final Optimised Parameters for Each Href Case	58

Nomenclature

Abbreviations & acronyms

Mpa Megapascal

mm Millimeters

°C Celcius Degree

2D/3D Two-Dimensional / Three-Dimensional

EBSD Electron Backscatter Diffraction

FE / FEM Finite Element / Finite Element Modelling

JC / J-C Johnson-Cook (Constitutive Model)

LM Levenberg-Marquardt (Algorithm)

ODB Output Database (Abaqus file format)

PH Precipitation-Hardening (e.g., 15-5PH steel)

QSD Quick-Stop Device

SPD Severe Plastic Deformation

SHPB Split Hopkinson Pressure Bar

T-Q/β Taylor-Quinney (Coefficient)

XRD X-Ray Diffraction

E Residual Errors

Machining & Simulation Parameters

- a_p Depth of Cut
- F_c Cutting Force
- F_f Feed Force
- *F*_p Penetration Force
- H_{ref} Uncut Chip Thickness
 - L_c Tool-Chip Contact Length
- T_c Deformed Chip Thickness
- *V_c* Cutting Speed
- μ Coefficient of Friction (Coulomb)
- J_{ij} Normalised Sensitivity Matrix
- J_i Jacobian Sensitivity Matrix

Material Behaviour Parameters Property

- A Yield Strength
- B Hardening Modulus

n Hardening exponent

m Themar Softening Exponent

C Strain-Rate Coefficient

 T_{melt} Melting Temperature

T_{room} Room Temperature

 $\dot{\epsilon}_0$ Reference Plastic Strain Rate

 ϵ_p Equivalent Plastic Strain

 $\dot{\epsilon}_p \hspace{1cm} \text{Equivalent Plastic Strain Rate} \\$

ρ Density

 σ Flow-Stress

 λ Damping Factor

Cutting Tools Features

CLA Clearance angle

CTA Cutting angle

EDG Edge length

ESR Edge sharpness radius

AMG Insert angle

REP Insert tip radius

KPR Tool lead angle (KAPR)

Chapter 1 Introduction

1.1. Background of Machining

Machining is one of the most widely used production techniques in industry for converting preformed blocks of metal into desired shapes with surface quality and dimensional accuracy [1]. During this Machining, which is a fundamental manufacturing process, there is severe deformation of the workpiece material in a very localized zone. Extreme machining conditions, including very high plastic strains (typically on the order of 1-4), high strain rates (up to roughly 106 s-1), and intense heating (temperatures close to melting) in the primary and secondary deformation zones, are applied to the material during these machining operations, like turning or milling [2]. These unique conditions lead to material behaviour that is markedly different from that observed in conventional quasi-static or low-rate material tests. As a result, standard material property data is not sufficient to describe how metals respond during machining. A constitutive model law, which is a mathematical model describing the flow stress of the material as a function of strain, strain rate, and temperature, is necessary to capture this behaviour for simulation [2]. Calibrating these constitutive models using experimental data has been used by several authors for metal cutting simulations. A reliable material behaviour law is crucial for realistic results in finite element (FE) machining simulations, as the choice of constitutive model has a significant impact on the accuracy of predictions (forces, chip formation, temperatures, etc) [2]. A widely used constitutive model is the Johnson–Cook (J–C) constitutive model, which incorporates key phenomena such as strain hardening, strain-rate sensitivity, and thermal softening in a straightforward analytic form and was developed especially to describe metals under high strains, high strain rates, and high temperatures, and for this reason, it has been integrated into many commercial machining simulation software packages [3]. Fundamentally, without an adequate constitutive law calibrated for extreme machining conditions, numerical simulations cannot accurately reproduce real cutting behaviour.

In recent years, finite element modelling of machining has become an essential tool for studying and optimizing manufacturing processes. The ability to simulate the cutting process enables engineers to predict critical outcomes, such as cutting forces, temperature fields, chip morphology, residual stresses in the machined part, and tool

wear. These simulations allow for a deeper understanding of the process and allow for "virtual experimentation" to complement physical trials [2]. Machining simulations are now frequently used to optimize cutting parameters, select or design cutting tools, and improve part quality, leading to increased productivity and reduced cost in manufacturing [2]. To achieve this purpose, the simulations must be accurate and precise, which in turn requires a suitable constitutive law for the workpiece material. A major challenge is that direct measurements of material behaviour at machining-level strain rates and temperatures are difficult, so the constitutive models often involve some empiricism and must be fit to whatever data is available. At this point, specific identification methods and data analysis become essential.

1.2. Problem Statement

It can be difficult to determine the proper material behaviour law under machining conditions. At higher strain rates and temperatures, stress-strain data can be obtained by conventional high-strain-rate material tests, such as Split Hopkinson Pressure Bar (SHPB) studies. In the direct approach, these tests would be carried out, and the constitutive equation would be fitted to the measured data for example, by calibrating the J-C model constants [2]. However, these tests have limitations: SHPB experiments typically achieve plastic strains less than 1 and strain rates on the order of $10^3 - 10^4$ s 1, which fall short of the extreme values encountered in actual cutting which are strains of 1 – 4 and strain rates up to $10^6 \, s^{-1}$ [2]. In other words, the deformation regime in machining far exceeds the regime covered by standard material tests, meaning that a constitutive model calibrated only on SHPB data must be extrapolated well beyond the tested range. This extrapolation introduces uncertainty and can lead to large prediction errors in machining simulations. Furthermore, multiple sets of model parameters often exist in the literature for the "same" material because the given alloy may exhibit different flow stress behaviour depending on factors like microstructure, heat treatment, or even strain path [3]. It is not always clear which set of constants is appropriate for a specific machining application, especially when those constants were obtained under different conditions.

However, the reference Johnson-Cook parameters often fail to predict actual machining outcomes such as chip morphology and cutting force, which my research study aims to tackle.

1.3. Aims and Objectives

This research aims to develop an inverse-identification and data-analysis framework for material-behaviour laws that enables accurate numerical simulation under machining conditions. Figure 1.1, shown below, presents the workflow for inverse identification and validation in machining simulation, outlining the pathway to achieving this aim. The ABAQUS finite element model is built with initial material behaviour parameters. The simulation is run, and its data, along with experimental machining data, is fed into the optimization algorithm (the inverse method). This process iteratively calibrates an optimized set of parameters for the material's constitutive behaviour law. This calibrated constitutive behaviour parameter is then subsequently deployed to accurately predict validated numerical machining conditions matching experimental machining, hence achieving the level of accuracy required for industrial applications.

To achieve the aim, the study will pursue the following specific objectives:

- To develop and validate a 2D finite element (FE) model of orthogonal cutting in ABAQUS/Explicit, incorporating a Johnson-Cook constitutive law.
- Implement an inverse-identification algorithm that calibrates those constitutive parameters along experimental machining data.
- Perform sensitivity analyses to quantify how individual parameters influence key simulation outputs.
- Conduct experimental orthogonal cutting tests to generate a comprehensive machining dataset for validation and calibration.
- Extend the framework from a two-dimensions (2D) to a hybrid three-dimensions (3D) orthogonal cutting simulation, varying the uncut-chip thickness to assess its impact on predictive accuracy.

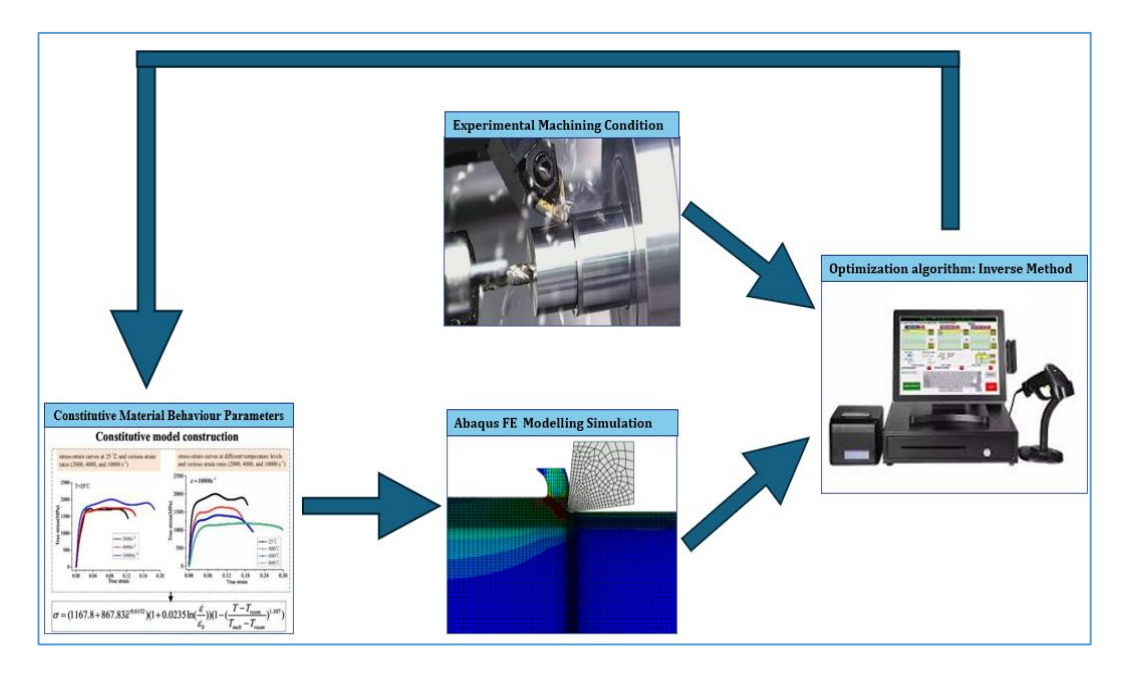


Figure 1.1: Integrated Experimental–Numerical Workflow for Inverse Identification in Machining

1.4. Industrial Relevance

The development of accurate numerical simulations for machining processes through inverse identification methods holds significant industrial importance across multiple high-value manufacturing sectors. This approach enables virtual process optimization while reducing costly physical trials [4], with particular benefits for aerospace, nuclear energy, automotive, and cutting tool industries [5]. The transformative impact of this methodology is conceptualized in Figure 1.2, which illustrates how the inverse identification process directly translates challenges from key industrial sectors into measurable benefits.



Figure 1.2: Industrial Relevance of Inverse Identification Methodology

In aerospace manufacturing, where components require machining of difficult-to-cut materials like titanium (Ti-6Al-4V) and nickel-based superalloys, inverse identification helps overcome limitations of traditional material models [6], These models often fail to predict real machining data for the material behaviour, leading to overly conservative process parameters [7]. By calibrating constitutive laws directly from machining data [8], Manufacturers like Airbus Helicopters have achieved 30% reductions in machining trials for critical rotor components [9].

Similarly, the nuclear energy sector benefits particularly from this approach when machining stainless steels (15-5PH) and zirconium alloys for reactor components [10]. With nuclear plants extending operations to 60+ years, predicting machining-induced residual stresses and microstructural changes becomes crucial [11]. Inverse methods incorporating X-ray Diffraction (XRD) residual stress data and Electron Backscatter Diffraction (EBSD) measurements [12]. Arrazola *et al.*, [13] have helped Framatome reduce Small Modular Reactor (SMR) fuel cladding pre-qualification costs by 25%. While in automotive manufacturers apply these techniques to optimize the machining of high-strength steels and aluminum alloys [14]. Virtual testing of chip breakability and tool wear across thousands of cutting cycles has enabled companies like Renault to reduce engine block machining costs by 18% [15].

These industrial applications demonstrate how inverse identification bridges the gap between academic research and practical manufacturing needs. By providing validated material models that reflect real machining conditions, the approach enables [9]:

- 30-50% reductions in physical trials for aerospace components
- 25% cost savings in nuclear component qualification
- 18% efficiency gains in automotive production
- 80% faster tool development cycles

The methodology's ability to predict previously unmeasurable variables (e.g., tool-chip interface temperatures, subsurface damage) while reducing material waste positions it as a transformative technology for modern manufacturing.

Chapter 2 Literature Review

2.1. Definition and Types of Machining (Orthogonal Cutting, Milling, Turning)

Machining is a family of manufacturing processes where excess material is removed from the workpiece in the form of chips to produce a finished component with the desired dimensions and surface finish [16]. In all machining operations, material removal is accomplished by forcing a tool against the workpiece and shearing the material plastically along a narrow zone, causing a chip to form and separate [17]. Common machining methods include turning, milling, drilling, and related processes. To analyze machining mechanics, researchers often consider an idealized orthogonal cutting model. In orthogonal cutting, the cutting edge of the tool is oriented perpendicular to the cutting direction, and there is no side flow of material [17]. Real machining operations like turning and milling are oblique three-dimensional cuts, but they can be conceptually broken down into orthogonal cutting at each tool contact point for understanding the deformation. In all, machining processes may vary in setup, but each involves severe shear deformation of the work material near the tool to form chips, which is why machining inherently falls under the domain of severe plastic deformation (SPD) processing [16]. SPD involves a material to a very large amount of plastic strain, leading to microstructural refinement in the material.

2.1.1. Severe Plastic Deformation Zones in Machining

During machining, the plastic deformation is highly localized into distinct zones around the cutting tool. [18]. These are commonly described as three deformation zones: primary, secondary, and tertiary as shown in Figure 2.1. The primary deformation zone is located ahead of the tool tip, within the workpiece material being cut [18]. Here, the material is intensely sheared and essentially, where the chip forms, the majority of plastic shear strain is generated in this

primary zone as the material transitions from the undeformed workpiece into the flowing chip [19]. Immediately after the primary shear, the chip continues to experience deformation and friction at the tool interface. This is the secondary deformation zone, located along the tool's rake face where the chip slides. In the secondary zone, the underside of the chip is subjected to additional shear and compressive stresses due to friction and contact with the tool [19]. The material in the chip's lower layers is further plastically deformed. This explains why the highest cutting temperatures are often observed at the tool-chip interface on the rake face [20]. Essentially, the chip material is first heated and sheared in the primary zone, then "burnished" and sheared again at the tool face in the secondary zone, generating intense heat from the combined plastic work and friction [20].

The tertiary deformation zone refers to the deformation that occurs in the thin layer of material on the finished surface, beneath the tool's clearance (flank) face [21]. As the cutting tool passes, it exerts pressure and causes severe plastic deformation in the surface layer of the workpiece that is left behind. The freshly machined surface thus contains a plastically deformed subsurface layer as a result of the cutting action [22]. This tertiary zone is critical to surface integrity; it can undergo strain hardening or microstructural transformations, and residual stresses may be introduced here. In other words, the quality and properties of the machined surface like fatigue life, corrosion resistance, etc. are largely dictated by what happens in this tertiary shear zone [23]. For example, severe shear in the tertiary zone can produce "swept" grain structures or even recrystallized grains in the outermost layer of the workpiece, and excessive heat in this zone may lead to tensile residual stresses or micro-cracks in extreme cases [24].

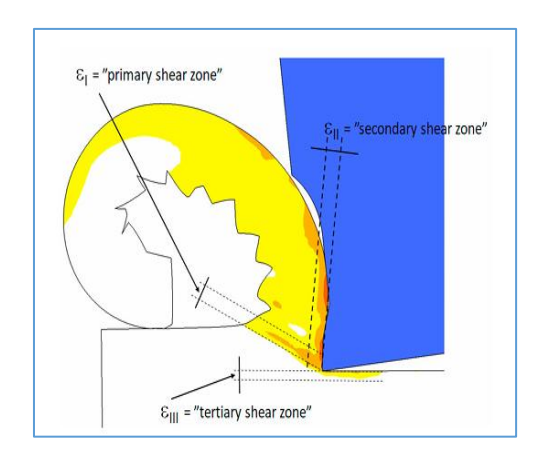


Figure 2.1: Shear zones in orthogonal cutting [23]

All three zones, which are the primary, secondary, and tertiary, involve severe plastic deformation of the metal, and together they explain how and where the cutting energy is dissipated as deformation and heat during machining.

The mode in which material flows and the chip form are central to understanding machining as an SPD process. In the primary shear zone, the work material undergoes intense shearing and essentially flows plastically around the cutting edge. If the material is ductile and cutting conditions are moderate, this flow is relatively continuous and produces a coherent, continuous chip as shown in Figure 2.2. However, under aggressive conditions, the deformation can become highly concentrated periodically, leading to segmented or serrated chips also seen in Figure 2.2. In such cases, the material in the shear zone undergoes cyclical instabilities (adiabatic shear bands) where it shears off in discrete chunks. The chip then exhibits a saw-tooth profile with alternating bands of heavily deformed material [22]. This serrated chip formation is another indication of the severe plastic flow, where the material may locally soften from temperature rise and shear in a narrow band, then repeat, resulting in a tooth-like chip morphology [22].

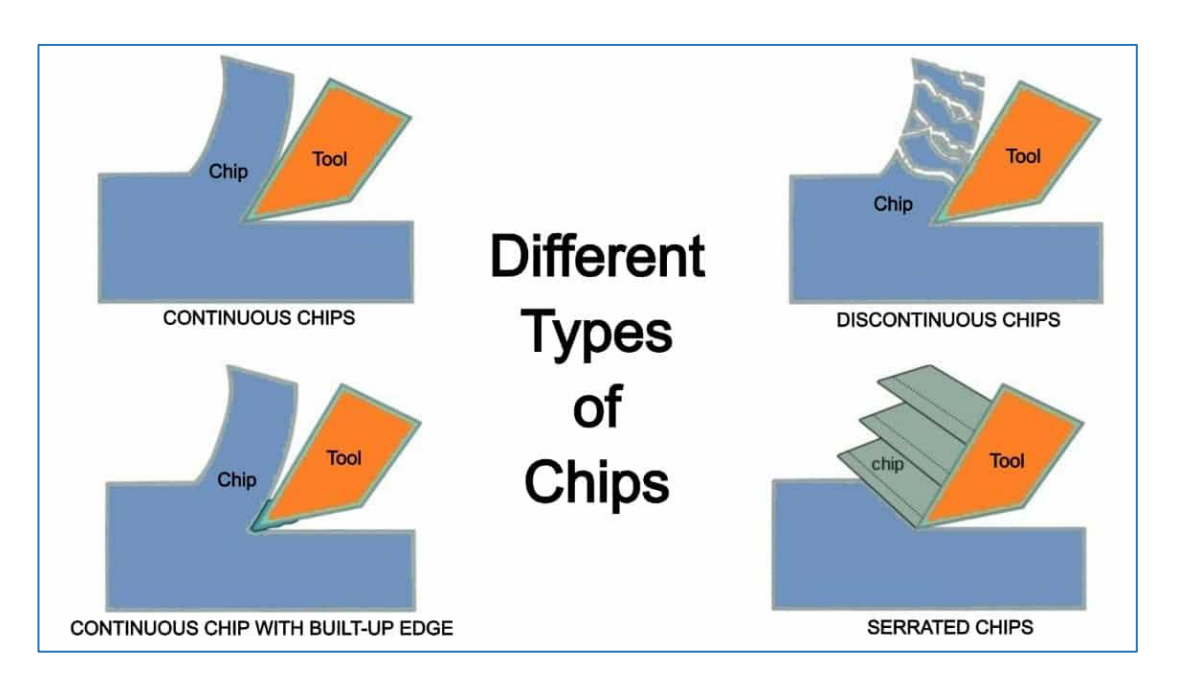


Figure 2.2: Illustration of the different types of chips formed in machining [22].

Whether continuous or serrated, the chip formation process involves substantial plastic flow. The material in the chip is usually highly strained and work-hardened by the time it exits the cutting zone. Indeed, measurements have shown shear strains in chips that are several times higher than the nominal strain imposed the chip essentially carries away much of the deformation imposed by the tool.

The material flow in front of the tool leads to chip formation via intense shear, and this process can refine grains and induce various transformations. Especially for difficult-to-cut or high-strength materials like 15-5PH stainless steel, the combination of high strain, high strain-rate, and temperature in machining produces significant microstructural evolution that must be understood. This lays the groundwork for later sections of this research, which will examine how this deformation and microstructural phenomena have been characterized in both experimental studies and simulations For instance, to optimize cutting of 15-5PH and similar alloys. By first reviewing the fundamental SPD characteristics of machining deformation zones, extreme strains, heat generation, and material flow leading to chip and microstructure changes, we establish a basis for understanding the advanced research on machining processes and their effects on materials [16]. This ability to create

refined microstructures via a single deformation pass is one reason machining is studied as a potential SPD technique for material processing.

The machined workpiece surface itself is also affected. In all, machining not only shapes the material by removing it, but in doing so, it alters the microstructure of both the removed chip and the remaining surface through SPD effects. The study to predict the mechanical behaviour of the materials flows needs to be accounted for within the frame of numerical simulation.

2.2. Mechanical Behaviour Laws in Metal Cutting

The accurate prediction of material behaviour under the extreme conditions of machining requires robust constitutive models. These mathematical formulations describe the flow stress of a material as a function of strain, strain rate, and temperature, capturing the complex interplay of strain hardening, strain-rate sensitivity, and thermal softening. The selection and calibration of an appropriate constitutive model are foundational to the fidelity of any numerical simulation of the machining process.

2.2.1. The Johnson-Cook Constitutive Model

The Johnson Cook (JC) Constitutive model is a widely used constitutive law expressing the flow stress of a metal as a product of strain hardening, strain-rate hardening, and thermal softening terms in numerical simulation [25]. The Johnson-Cook Constitutive equation as shown in Eq. (2.1)

$$\sigma = \underbrace{(A + B\varepsilon_p^n)}_{\text{Strain hardening}} \underbrace{\left(1 + C\ln\frac{\dot{\varepsilon}_p}{\dot{\varepsilon}_0}\right)}_{\text{Strain rate hardening}} \underbrace{\left(1 - \left[\frac{T - T_{room}}{T_{melt} - T_{room}}\right]^m\right)}_{\text{Thermal softening}}$$
(2.1)

Where; σ Is the flow stress, ϵ_p the equivalent plastic strain, $\dot{\epsilon}_p$ the plastic strain rate, with $\dot{\epsilon}_0$ As the reference strain rate, T the material temperature, T_{room} a reference temperature, and T_{melt} The melting temperature. The five material constants in this model (A, B, n, m, C) characterize the material behaviour [28]:

- **A:** Yield stress of the material at the reference temperature and reference (quasi-static) strain rate.
- **B:** Strain hardening coefficient, determining the increase in flow stress with plastic strain.
- **n**: Strain hardening exponent, which governs the curvature of the stress-strain

- relationship in the plastic regime.
- **C:** Strain-rate sensitivity coefficient, controlling how much the flow stress increases with higher strain rate.
- \mathbf{m} : Thermal softening exponent, describing how the material strength decreases as the temperature approaches T_{melt} (the material melting temperature).

The Johnson-Cook model captures a material's thermo-viscoplastic behaviour by decoupling the effects of strain, strain rate, and temperature in a multiplicative form [25]. This means the material's strengthening from cold work (strain hardening), the additional resistance under faster loading (strain-rate hardening), and the weakening at elevated temperatures (thermal softening) are all accounted for independently. Such a formulation is advantageous for metal cutting simulations, as machining involves severe plastic deformation at high strain rates and temperatures. The JC model's small number of parameters and straightforward calibration have made it extremely popular for machining applications [26]. Indeed, surveys indicate that the Johnson–Cook law on original and modified forms has been employed in the majority of material models for machining simulations over the past decade [25].

Despite its utility, the Johnson-Cook model has known limitations. Being empirical, it may produce inaccurate results if extrapolated beyond the range of calibration data [25]. The model assumes the effects of strain hardening, rate hardening, and thermal softening are independent and without any history coupling. This simplistic decoupling means Johnson-Cook cannot capture certain metallurgical phenomena like dynamic strain aging or phase transformations and may misestimate behaviour under complex loading paths. For example, the standard Johnson-Cook formulation lacks any intrinsic flow-softening mechanism aside from thermal softening. Consequently, it often fails to predict the flow stress drop associated with adiabatic shear banding or dynamic recrystallization, which are important in high-speed cutting of some alloys [22]. Comparative studies have shown that the original Johnson-Cook model tends to overpredict flow stress at elevated temperatures unless an additional softening term is introduced [27]. As a result, simulations using an unmodified JC law sometimes produce continuous chip formation, whereas real experiments show segmented or serrated chip patterns due to localized material softening. Researchers have responded by proposing various modified Johnson-Cook models or hybrid constitutive laws that include extra softening terms or state variables to improve accuracy. Nonetheless, the

base JC model remains a common baseline in machining simulations, and its parameters must be chosen carefully. For instance, studies have found that different sets of JC constants for the same material can significantly affect predicted cutting forces, temperatures, and chip morphology [22], underscoring the importance of proper parameter identification and validation against experiments.

2.2.2. Friction and Taylor-Quinney Coefficient in Machining

The interaction at the tool-chip interface is governed by two critical phenomena: friction and heat generation. Their accurate representation is paramount for realistic simulations, as they directly influence cutting forces, chip morphology, tool wear, and the thermal field within the workpiece and chip. We would detail at both the role of the friction coefficient and Taylor-Quinney below on the Tool-Chip interface.

Role of Friction at the Tool-Chip Interface:

Friction between the cutting tool and the chip plays a crucial role in metal cutting. The tool-chip interface friction significantly influences cutting forces, chip formation, and heat generation during machining. A large portion of the cutting energy is dissipated as frictional heat at this interface, often accounting for a major share of the overall heat in machining. The rise in temperature due to friction can soften the work material, but also accelerate tool wear and may degrade the machined surface quality [22]. Friction conditions (e.g. changes in lubrication, tool coating, or cutting speed) can lead to fluctuations in cutting forces and affect chip morphology and stability. This is especially pronounced in materials with low thermal conductivity (like titanium alloys), where frictional heating cannot dissipate quickly and thus exacerbates thermal effects and tool wear [22].

In finite element modelling of machining, the tool-chip friction is typically represented by simplified laws. The most straightforward and widely used model is Coulomb's law with a constant friction coefficient, μ [22]. This model is easy to implement and is available in most commercial FE software, so many researchers assume a constant often on the order of 0.1– 0.5 value to simulate sliding friction at the interface. While convenient, a pure Coulomb model with a single μ may oversimplify reality, since the apparent friction can vary along the contact length and depends on local pressure, sliding speed, and temperature. An alternative approach commonly used in machining simulations is the constant shear friction model, which imposes an upper limit on the

frictional shear stress.

Taylor-Quinney Coefficient:

The Taylor-Quinney coefficient which is denoted as β is a material parameter that defines the fraction of plastic work converted into heat during deformation [28]. In any plastic deformation process, part of the mechanical work is stored in the material, while the remainder is dissipated as heat. The Taylor-Quinney coefficient quantifies this balance, where $\beta=0$ would mean all plastic work is stored (no heat generation), whereas $\beta=1$ means all plastic work is instantly converted to heat. In machining, deformation is highly rapid and often close to adiabatic, so it is commonly assumed that a large majority of the plastic work manifests as heat. Many machining simulations simply assume $\beta\approx0.9$, where 90% conversion to heat as a default value [28]. This implies that most of the energy expended in plastically deforming the chip is transformed into thermal energy, which then raises the temperature of the chip, tool, and workpiece interface. The partitioning of this heat between the tool and the chip is a critical modeling consideration, as illustrated in Figure 2.3.

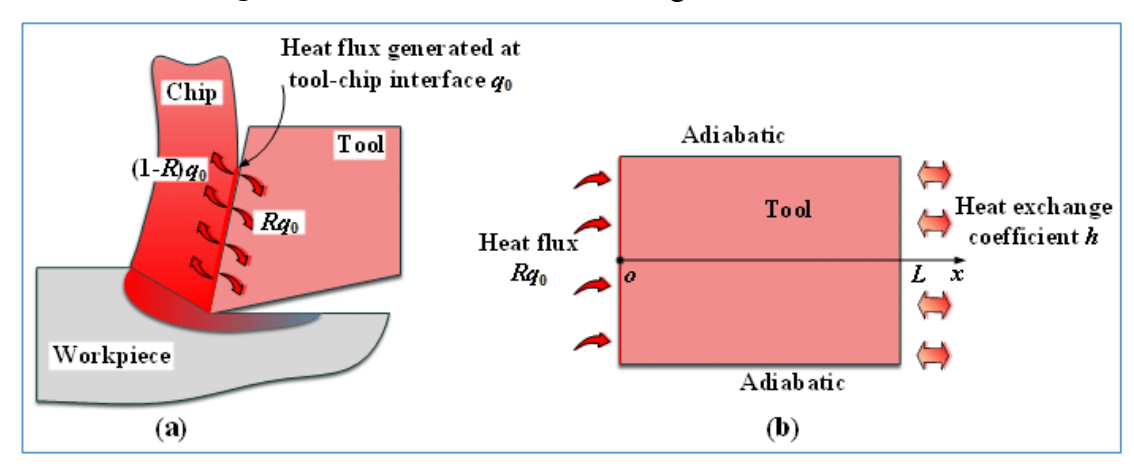


Figure 2.3: Model of heat partitioning at the tool-chip interface [29].

The total heat flux (q_0) generated by friction and plastic deformation is split, with a portion (Rq_0) entering the tool and the remainder $(1-R)q_0$ being carried away by the chip. The boundary conditions, including adiabatic surfaces and heat exchange, are critical for accurate thermal simulation[29]. The Taylor-Quinney coefficient is thus a key factor in heat generation modelling: it directly scales how much heat is added per unit of plastic work in the primary shear zone and secondary deformation (tool-chip interface) zone. A higher β leads to more intense heating for the same deformation,

affecting predictions of cutting temperature, tool wear, and potential thermal damage to the work material.

Although a constant $\beta \approx \text{ of } 0.9$ is often used for metals, studies have shown that the Taylor-Quinney coefficient is not truly constant and can vary with material and deformation conditions [28]. In classical experiments, Taylor and Quinney themselves observed that the fraction of plastic work converted to heat tends to increase with ongoing deformation. Recent investigations have quantified this variability: for example, high-speed deformation tests on steel have found β starting around 0.5 (50%) of work as heat) at the onset of yielding and rising to 0.95 at large strains. This increase is explained by the material's diminishing capacity to store further strain energy as deformation progresses. Early plastic work goes into generating defects (stored energy), but as the material hardens and saturates with defects, additional work is more fully dissipated as heat. Moreover, the effective β can differ widely between materials. Zubelewicz compiled data showing average Taylor-Quinney values ranging from about 0.2 up to 0.9 for different metals under dynamic loading [30]. High-strength alloys, for instance, might store a larger fraction of work (lower β) compared to softer metals at similar strain rates. Strain rate and temperature also influence β at higher strain rates, adiabatic conditions prevail, and β tends to be higher, whereas at lower rates or with active thermal conduction, a greater portion of work can be temporarily stored. These findings imply that assuming a universal β = 0.9 can sometimes misrepresent heat generation. Nonetheless, in practical machining simulations, β is often kept at 0.9 in the absence of specific experimental data, as this value has been a reasonable approximation for many metals undergoing rapid deformation [28]. Researchers are increasingly aware of Taylor-Quinney variability, and some have developed methods to measure or even dynamically adjust β in simulations [28]. However, the Taylor-Quinney coefficient provides the link between mechanical work and thermal effects in machining, and understanding its range helps in assessing the accuracy of temperature predictions and the potential for thermal softening or damage during the cutting process.

2.3. Experimental Data in Machining: Chip Geometry, and Forces

Experimental data serves as the essential link between theoretical models and physical reality. In machining research, measurements of chip geometry and cutting forces

provide the fundamental validation metrics for evaluating and calibrating numerical simulations. These datasets offer tangible evidence of the material's response to the severe conditions of cutting.

2.3.1. Chip Thickness and Contact Length in Machining

Chip geometry, specifically the deformed chip thickness (T_c) and the tool-chip contact length (L_c) , are direct outcomes of the plastic deformation process and provide critical insight into the mechanics of cutting. The deformed chip thickness reflects the material's shear deformation and directly relates to the shear plane angle and compression ratio. A higher chip thickness generally indicates a smaller shear angle and more intense plastic deformation, whereas thinner chips correspond to a larger shear angle and potentially easier cutting. For example, [31] observed that at very high cutting speeds, V_c above 450 m/min the chip became notably thinner (increased shear angle), and the cutting forces reached minimum values. This exemplifies how chip thickness is coupled to cutting mechanics, conditions that promote thinner chips can reduce cutting resistance. The tool-chip contact length, which is the length of the rake face in contact with the chip, is equally important. It determines the interaction in the secondary cutting zone, governing friction and heat transfer between tool and chip [31]. A longer contact length typically means a larger area for friction, higher cutting temperatures, and more tool wear, whereas a shorter contact may indicate quicker chip separation. Indeed, contact length has a significant influence on tool temperature and wear, where an increased contact length raises tool interface temperature, accelerating wear mechanisms. Because of these effects, contact length is widely used as a key parameter in analytical cutting models and as a check on machining simulations [31]. However, chip thickness captures the severity of shear deformation and chip compression, while contact length encapsulates the size of the tool-chip engagement zone; both are essential for characterizing machining responses such as forces, heat, and tool wear. All of these for the Chip Thickness and Tool-Chip Contact Length Length are shown on the Geometry of orthogonal cutting as shown in Figure 2.4.

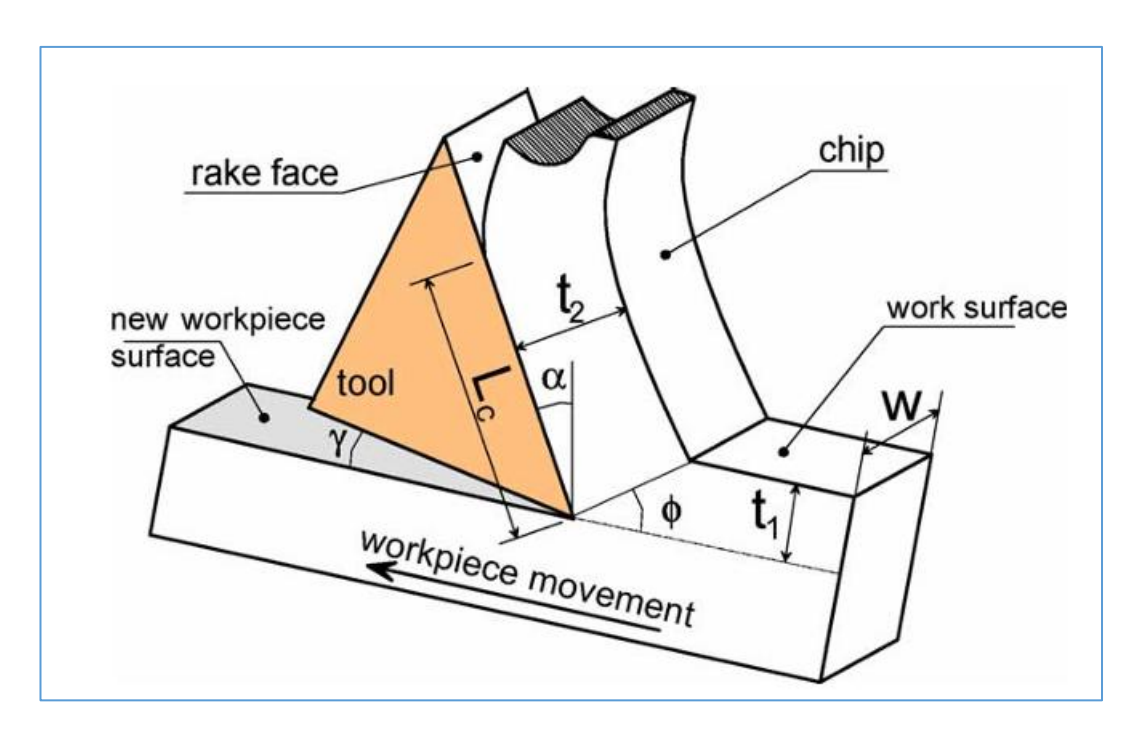


Figure 2.4 : Geometry of orthogonal cutting [32].

Accurate measurement of chip thickness and contact length is vital for both experimental analysis and for providing validation data to simulations. Chip thickness is commonly measured post-machining by collecting the chips and examining their cross-section. A micrometre or optical microscope can be used to measure the thickness of representative chip segments. For segmented or serrated chips, high-resolution imaging allows measurement of segment peak thickness, valley thickness, and serration period. In many cases, multiple chip samples are measured to obtain an average chip thickness for a given cutting condition [32].

Measuring the tool-chip contact length is more challenging, as it involves capturing an interface that is typically hidden during cutting and may change with time. Several established methods exist and one traditional approach is the use of a quick-stop device (QSD), which suddenly halts the cut and freezes the chip still attached to the tool. This allows the chip root and the portion of the chip in contact with the rake face to be examined. Using QSD, researchers historically measured contact lengths and even observed the primary shear zone geometry. However, quick-stop devices can be complex to implement at high cutting speeds and may perturb the process [33].

2.3.2. Force Measurement in Machining

The measurement of cutting forces is crucial for machining experimentation. In a typical cutting test, the forces are resolved into orthogonal components. The primary cutting force, F_c acts in the direction of cutting velocity, which is tangential to the

workpiece in turning, or along the tool feed in orthogonal cutting. This is usually the largest force component and directly relates to the energy required for material removal. The penetration force, F_p is the force pushing the tool into the workpiece. In an orthogonal cutting setup, this corresponds to the force normal to the cut surface, sometimes called the passive force depending on the context. Many authors refer to the force into the work material (normal to the cutting plane) as the thrust force (analogous to penetration force), and the in-feed direction force as the penetration force. In summary, a 3D cutting process like turning yields three components: cutting force F_c , feed force F_f , and passive (penetration) force F_p . These components are routinely measured with a dynamometer [33], as shown in the experimental setup in Figure 2.5.

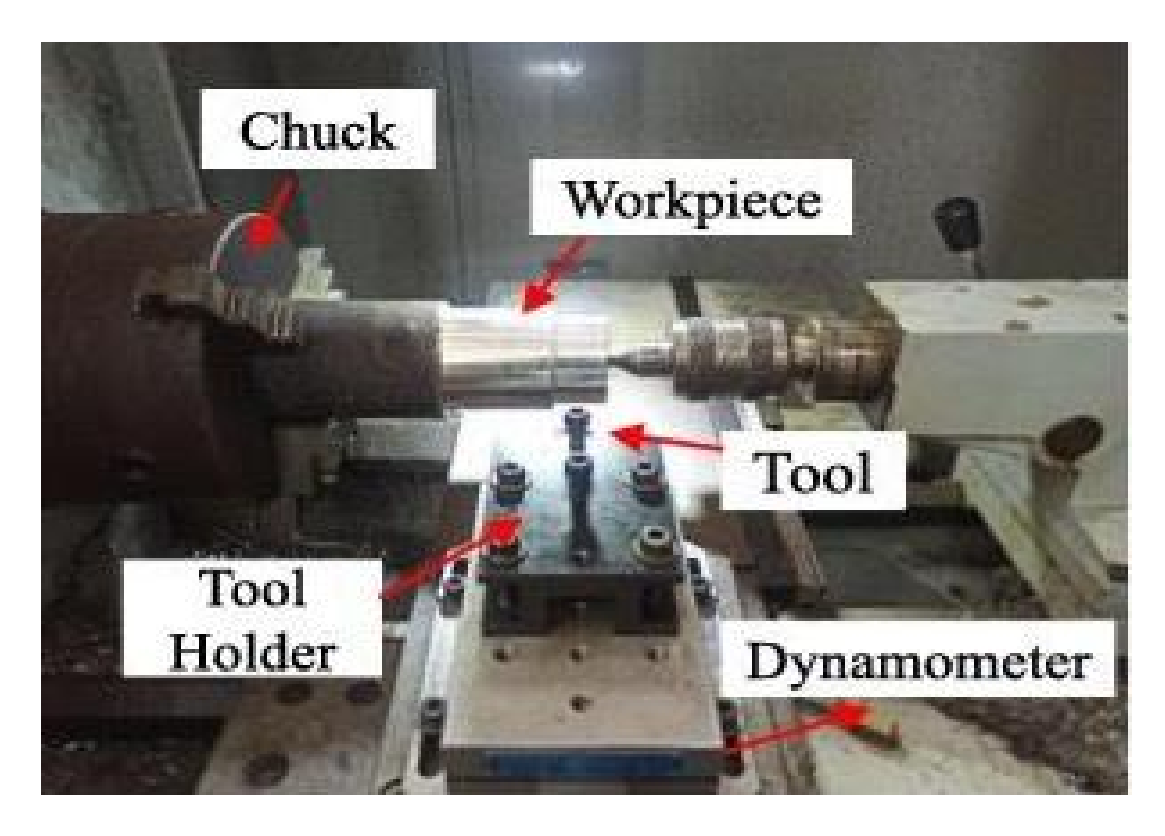


Figure 2.5: Experimental setup for Cutting Force Measurement [33].

Cutting forces are typically measured using piezoelectric dynamometers mounted on the machine. These devices e.g. Kistler dynamometers can resolve forces in X, Y, Z directions with high frequency response. The force signals are recorded, filtered, and the steady-state values of F_c , F_p , and F_f are obtained for each cutting test. All this experimental setup for measuring the Force are shown in Figure 2.6.

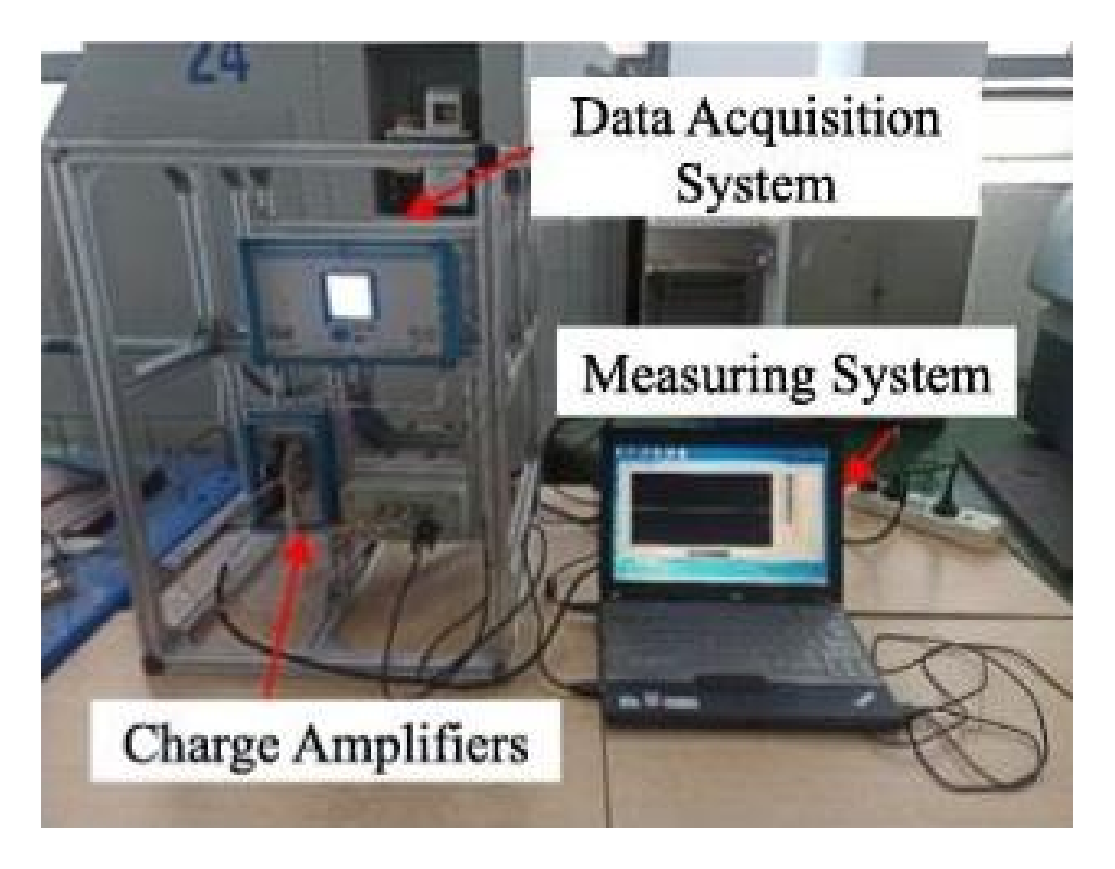


Figure 2.6: Cutting force measurement system [33].

One of the most important uses of the above experimental data is in the inverse identification of material behavior laws and the calibration of finite element (FE) machining simulations. In machining FE models which often employ constitutive laws like Johnson-Cook, Zerilli-Armstrong, etc., and friction models for the tool-chip interface, many material parameters are not known with certainty. Direct high-strainrate testing of materials at cutting conditions is difficult, so researchers rely on inverse methods which is essentially tuning the model parameters so that the simulation outputs match the experimental measurements. Cutting forces are a primary calibration target they reflect the overall energy and resistance of cutting and are relatively easy to measure accurately. Most simulation validation papers will report that the simulated cutting force and penetration force are compared to experimental values as a matter of course [34]. For example, [34] note that in orthogonal cutting simulation of Ti-6Al-4V, the cutting force, feed force, and chip thickness are usually analyzed and compared with the experimental results. Achieving good agreement in these forces is often the first goal of calibration. The penetration forces are also important, especially for capturing the correct stress state on the tool and workpiece. However, many researchers give slightly higher priority to the cutting force during

calibration, since it dominates in magnitude and is crucial for power predictions and tool load. In multi-objective optimization approaches for parameter identification, it is common to weight the cutting force error more heavily than the secondary force or chip thickness errors. This industrially reflects that an error in cutting force has significant consequences (tool fracture, machine overload, etc.), whereas moderate errors in chip thickness might be tolerated if forces are right [34].

That said, chip morphology has become increasingly important in inverse identification, to ensure the model is capturing the plastic deformation behaviour correctly. A simulation could conceivably get the forces right with a wrong combination of flow stress and friction they can compensate each other, but the chip geometry might reveal the discrepancy. Thus, recent studies incorporate chip thickness as an objective in the calibration. For instance, [34] applied an efficient global optimization algorithm to calibrate a Johnson-Cook model for Ti-6Al-4V, and their identified parameter set predicted cutting force within 2% and chip thickness within 11% of experiments, while an initial parameter set had much larger chip thickness error. [35] explicitly advocate using multiple observables to overcome non-uniqueness in inverse material parameter identification. In their approach, they simultaneously considered cutting force, penetration force, chip thickness, chip temperature, and even chip curvature (radius) as target outputs. By increasing the number of process observables to include thermal and geometric data, they ensured that the material model (Johnson-Cook parameters) was not only fitting the forces but also the chip formation characteristics. This multicriteria approach is vital because different parameter sets can sometimes produce similar force results but differ in predicted chip shape or temperature. Using chip thickness and shape as additional criteria penalizes unphysical solutions and yields a more robust calibration of the constitutive law.

The tool-chip contact length is another observable used in some inverse analyses, particularly to calibrate friction parameters at the tool-chip interface. Since contact length is sensitive to the friction coefficient and the normal stress distribution on the rake face, matching the observed contact length can help tune those aspects of the simulation. [31] for example, compared FE simulations of orthogonal cutting to experiments and reported that after adjusting the constitutive equation parameters, the simulated contact length agreed within 12% of the experimental values across a range of cutting speeds, depths, and rake angles. This level of agreement in contact length alongside force agreement gives confidence that the friction and material flow stress were correctly set in the model.

Over the last decade, numerous researchers have presented inverse identification case studies using experimental force and chip data. [34] were among the early to extract Johnson–Cook parameters from machining tests using an optimization algorithm. [36] used Oxley's analytical machining theory in an inverse manner to determine constitutive equations, matching predicted forces to experimental cutting forces. More recently, [34] have published several papers on automated optimization for material model parameters, considering multiple outputs and using algorithms from downhill simplex to particle swarm optimization. In each case, experimental data usually a set of forces and sometimes chip thickness or residuals form the objective function to minimize.

Importantly, experimental data from challenging materials like precipitation-hardened (PH) stainless steels have served as proving grounds for these techniques. 15-5PH and 17-4PH stainless steels, known for their high strength and relatively poor machinability, have been the subject of recent machining studies to generate such data. [37] examined 15-5PH cutting forces and chip characteristics under various conditions; such data is invaluable for calibrating models for aerospace-grade materials. [38] specifically investigated turning of 15-5PH and used a hybrid simulation model driven by experimental inputs, they replaced the actual chip formation in the FE model with imposed thermal/mechanical loads calibrated from experimental force, chip thickness, and contact length measurements. The very name "hybrid model" in their work refers to melding experimental data with numerical simulation. By inputting the measured forces, chip thickness, and contact length into their model, they could simulate residual stress outcomes much faster than a full physical cutting simulation, with good accuracy [34]. This exemplifies how experimental machining data are ultimately fed into simulation frameworks to identify material behavior and to calibrate simulations for predictive use. In the end, the results of machining simulations whether for predicting forces, chip morphology, or residual stresses hinges on how well we have tuned them to match reality. And for that tuning, high-quality experimental data on chip thickness, contact length, and cutting forces are critical. They serve as the benchmark for simulation accuracy and the target for inverse identification algorithms, ensuring that the constitutive models governing material plasticity and friction in the simulation truly reflect the physical behavior observed in machining [32].

2.4. Numerical Simulation of Machining

Numerical simulation using finite element methods (FEM) has become a widely adopted tool for studying metal cutting and machining processes [39]. By modelling chip formation and tool-workpiece interaction, FEM allows researchers to analyse the complex thermo-mechanical conditions in the cutting zone and predict key outputs such as cutting forces, temperatures, stress distributions, chip morphology, surface integrity, and even tool wear [39]. Commercial FE software like Abaqus/Explicit is frequently used to simulate machining operations due to its capability to handle the large deformations, high strain rates, and contact/friction conditions inherent in cutting. Users often employ Python scripting in Abaqus to automate simulation workflows and parameter studies, enabling integration of FEM simulations with custom algorithms.

Accurate material modelling is critical in machining simulations [40]. The workpiece material is typically characterized by an empirical constitutive law that can capture strain hardening, strain-rate sensitivity, and thermal softening at the extreme conditions of machining. One of the most widely used models is the Johnson-Cook constitutive model, which expresses the flow stress as a product of factors dependent on plastic strain, strain rate, and temperature [41]. The JC model introduces five parameters that must be tuned for the specific material. It has gained popularity due to its simplicity and its suitability for large strain, high strain-rate, high temperature deformation, making it a common choice for simulating processes [42]. However, the analysis of any machining simulation hinges on using correct constitutive parameters for the workpiece material [43]. As a result, direct use of parameter values extrapolated from milder tests can be inaccurate for simulations of machining. This gap has motivated researchers to pursue inverse identification approaches, where material parameters are calibrated from machining process data itself by comparing simulation results with experimental measurements.

2.5. Inverse Identification Methods

Inverse identification refers to the process of determining unknown model parameters by inverting experimental observations i.e. finding the parameters that cause a simulation to reproduce measured outcomes. In the context of machining, this means adjusting material properties so that the FEM simulation of a cutting process yields results (cutting forces, chip shape, temperatures, etc.) that closely match those

observed in real machining trials [44]. Unlike a direct analytical solution, this is generally formulated as a nonlinear optimization problem: an *objective function* quantifies the discrepancy between simulation predictions and experimental data, and an algorithm iteratively updates the material constants to minimize this discrepancy [45].

A variety of inverse identification strategies have been reported in the literature since 2010. The simplest approach is a manual or brute-force search: some researchers have systematically varied the JC parameters by trial and error until the simulation outputs fall within an acceptable error range of the measurements. [45] followed this kind of approach, allowing each initial JC constant to vary up to ±50% of its literature value in order to reduce the error in predicted cutting forces and shear zone temperatures. A more methodical strategy was demonstrated by [46], who employed a *Kalman filter* based iterative update to identify five JC parameters from orthogonal cutting data. Their Kalman filter treated the parameter determination as a state estimation problem, updating the constants in an iterative manner using the prediction error, and successfully converged to a set of flow stress constants that improved simulation accuracy [45].

Many researchers have formulated the inverse problem explicitly and solved it with numerical optimization algorithms. One popular choice is the Levenberg-Marquardt (LM) algorithm, which is a damped least-squares optimization method closely related to the Gauss-Newton approach and by extension to Newton-Raphson for solving nonlinear problems. [47] appears to have been an early adopter of this, using the Levenberg-Marquardt method to calibrate JC parameters in a metal forming context. In recent years, LM has been applied in machining simulations as well. [44] implemented an inverse identification of JC constants from machining by coupling an Abaqus FE model with a Levenberg-Marquardt optimizer. In their procedure, after each simulation run the algorithm computes the objective function gradient and updates the parameter estimates, gradually reducing the error between simulated and observed chip formation behaviour.

Aside from gradient-based algorithms, researchers have also explored evolutionary and heuristic optimization techniques for inverse identification. These methods do not require gradient information and can be more robust in searching a complex parameter space, at the cost of more function evaluations. For instance, [40] used a firefly algorithm to fit a modified Johnson-Cook model for Ti-6Al-4V cutting, achieving good results in matching cutting forces. [48] investigated particle swarm optimization (PSO)

for determining JC parameters from machining simulations and demonstrated it could converge to a near-optimal solution within a limited number of simulation iterations by smartly "swarming" around promising regions of the parameter space. Other works have applied genetic algorithms, downhill simplex methods, and other optimization routines to this inverse problem, reflecting a growing interest in techniques that improve the robustness and efficiency of material parameter identification for machining. Regardless of the specific algorithm, the trend is clear that inverse identification has become a key tool to tune constitutive models so that FEM simulations can reliably predict machining performance under modern conditions [40].

2.6. Gradient Sensitivity & Perturbation Techniques

A critical component of any gradient-based identification method is the evaluation of sensitivities, how sensitive the simulation outputs are to changes in each model parameter. These sensitivities form the Jacobian matrix required for Newton, Gauss-Newton or Levenberg-Marquardt updates. In complex machining simulations, an analytical expression for the gradient is typically unavailable, so researchers resort to perturbation techniques to estimate sensitivities. This involves perturbing one Johnson-Cook parameter at a time by a small amount e.g. a few percent and re-running the simulation to observe how the outputs change in response [40]. By computing the incremental change in outputs over the incremental change in parameter, a finitedifference approximation of the partial derivative is obtained. Repeating this for each parameter yields the Jacobian matrix that feeds into the optimization algorithm. Although this approach can be computationally expensive (requiring multiple simulations per iteration), it is straightforward to implement and has been widely used. For instance, [40] performed a systematic sensitivity analysis by varying each JC parameter (A, B, n, C, m) by ±20% and recording the effects on cutting forces and chip geometry. Such one-at-a-time perturbations revealed which parameters have the strongest influence on different aspects of the machining process, guiding the inverse identification and highlighting where more precise calibration is needed.

The influence of one parameter may depend on the values of others, meaning that adjusting two parameters simultaneously can produce non-additive effects on outputs [49]. For example, a combination of a higher hardening modulus, B, together with a higher thermal softening, m, might counteract or amplify each other's influence in non-intuitive ways on cutting forces and chip geometry. [50] compared multiple Johnson-Cook datasets in the literature and found that certain combinations of parameters can

yield similar cutting force predictions, even if individual parameters differ significantly. This reinforces the need for performing global sensitivity analyses or using design-of-experiments approaches to probe the parameter space more fully, rather than varying one factor at a time. In practice, when implementing a gradient-based inverse identification, one must ensure that the chosen experimental observables provide enough information to distinguish the effects of each parameter. For instance, measuring both forces and chip morphology provides more constraints than measuring forces alone, improving parameter identifiability [48]. Likewise, using several cutting test conditions can help decouple parameters that have overlapping effects under a single condition. Modern approaches thus often combine multi-objective calibration with multi-condition data to obtain a robust solution.

Notably, gradient sensitivity and perturbation techniques form the backbone of calibration algorithms by providing the necessary derivative information. They not only drive the numerical optimization but also offer physical insight into the machining process itself revealing which material properties most strongly control outcomes like force, temperature, and chip formation.

2.7. Research Gap

To position my work within the scope of machining optimisation, I have identified six key studies that represent the state-of-the-art as shown in Table 2.1. This table compares their methods, targets, and goals, and directly outlines the specific contributions my thesis makes to advance the research.

Study	Method	Target Data		Goal	Research Gap Filled
Kugalur	Efficient	Cutting		Minimize error for	Extend to more observables
Palanisamy	Global	force,	feed	Ti-6Al-4V; reduce	(contact length, chip
et al. (2022)	Optimizati	force,	chip	manual effort	thickness) to address non-
[33]	on	thickness			uniqueness; calibrate
	(Bayesian				constitutive and friction
	/Gaussian				models under a bounded
	Process,				global search.
	GP)				

Hardt &	Downhill	Forces, chip	Improve accuracy	Include friction Taylor-
Bergs (2021)	Simplex	temp., chip	and study non-	Quinney and a global
[34]	Algorithm	geometry	uniqueness of JC	optimizer; add multi-
			parameters	condition constraints to
				shrink solution space and
				report uncertainty.
Aguret et al.	Kalman	Forces,	Find material	Uses more data (forces, chip
(2014) [49]	Filter	Temperatur	constants from	thickness, contact length) to
		e	tests	reduce error discrepancy and
				improve accuracy.
Shrot & Ker	Levenberg	Chip shape,	Robust parameter	Implements a more stable,
(2011) [49]	-	Forces	update for	bounded method and
	Marquardt		simulations	validates it on more scenarios
				of cut section.
Shrot &	Particle	Forces	Avoid local	Combines robust search with
Baker	Swarm	(from	minima with	a faster, guided method and
(2011) [49]	Optimizati	simulation)	global search	uses multiple data types for
	on			better results.
Oxley Model	Analytical	Cutting	Quick inversion	Uses a full, realistic
(2013) [49]	Inverse	Forces	without	simulation calibrated against
			simulation	force and chip geometry for
				greater accuracy.

Table 2.1: Summary of Research Gaps and Thesis Contributions

Chapter 3 Methodology

3.1. Overview of the Methodological Approach

This research develops an integrated computational-experimental framework for calibrating Johnson-Cook constitutive parameters and the Taylor-Quinney coefficient under machining conditions for several undeformed chip thicknesses from the 2D simulation to the 3D. The methodology systematically combines orthogonal cutting experiments with finite element modeling and inverse optimization in a closed-loop calibration process, as illustrated in Figure 3.1 and Figure 3.2

The approach begins with controlled orthogonal machining experiments that provide quantitative measurements of chip geometry (thickness and contact length), penetration force, and cutting forces. These experimental results serve as critical calibration targets for numerical model development. A 2D finite element model is then developed in Abaqus, accurately replicating the machining process with precise boundary conditions, material properties, and friction modeling. Workpiece material behavior is defined using the Johnson-Cook constitutive law, while the cutting tool is modeled as rigid to simplify contact interactions.

Critically, while the Johnson-Cook parameters and Taylor-Quinney coefficient are initialized using reference values from literature, these values serve only as a starting point. At the core of the methodology is a Python-driven optimization loop that iteratively adjusts the Johnson-Cook parameters along with the Taylor-Quinney coefficient (β = 0.6-0.95). The Levenberg-Marquardt algorithm is employed for efficient parameter identification, incorporating finite difference-based sensitivity analysis to quantify each parameter's influence on machining outputs. This optimization process minimizes discrepancies between simulation results and experimental data across multiple criteria, including chip geometry and forces.

Upon achieving convergence in the 2D model, the calibrated parameters undergo rigorous validation against independent experimental results. The validated model is then extended to a 3D hybrid configuration for industrial applications. The methodologies are robust due to their integration of experimental data with numerical simulations, enabling accurate parameter identification under extreme machining conditions. Figure 3.1 presents the Python-Abaqus optimization framework, detailing

the automated workflow from experimental data input through parameter perturbation, sensitivity analysis, and iterative updates to final validation.

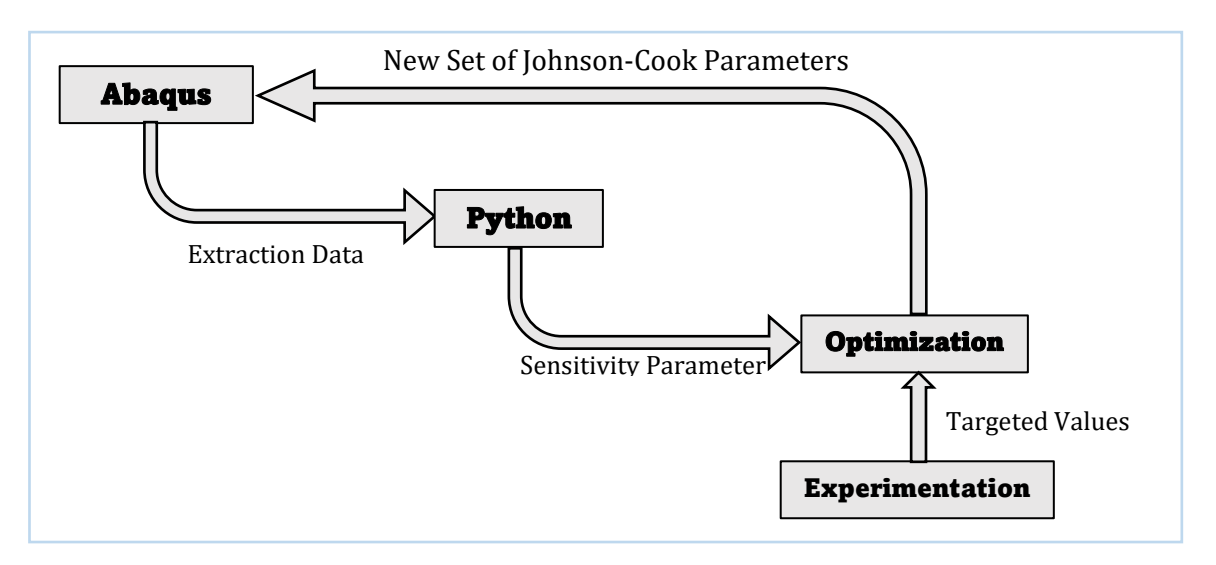


Figure 3.1 : Python-Abaqus optimization framework, highlighting Experimentation, sensitivity analysis, and iterative updates.

While for Figure 3.2 illustrates the complete integrated workflow, showing the progression from 2D model development and parameter extraction to 3D model extension and industrial application validation.

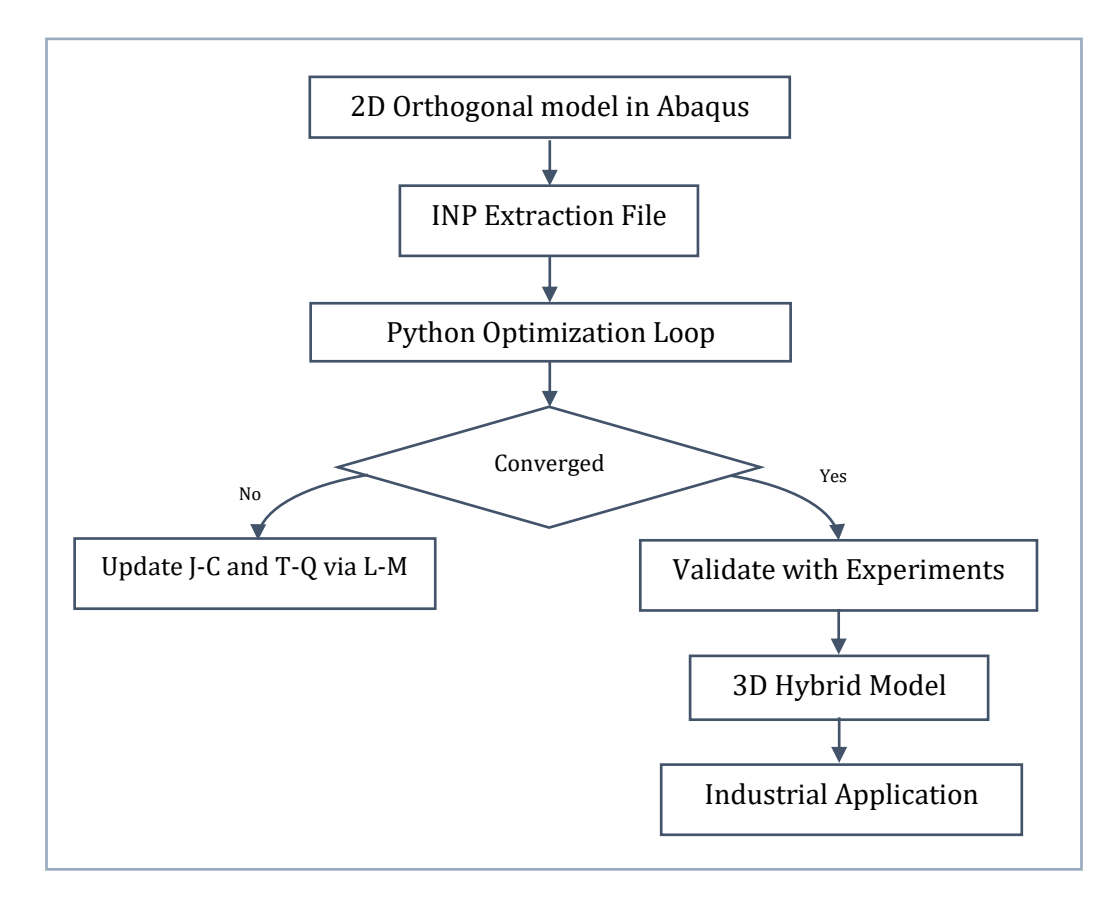


Figure 3.2 : Workflow of the integrated experimental-numerical calibration process, from 2D FE modelling to 3D validation

This approach establishes a rigorous algorithm for material model calibration in machining simulations, combining computational efficiency with experimentation. The subsequent sections provide detailed explanations of each methodological component: Experimental design approach in Section 3.2, Numerical Simulation with Abaqus in Section 3.3, Python-Abaqus Coupling in Section 3.4, and 2D to 3D simulation optimisation workflow in Section 3.5.

3.2. Experimental Approach

The experimental machining data generated in this research are designed to produce a reliable dataset for the inverse identification of material constitutive parameters. While direct experimentation on 15-5PH was not used within the scope of this work, a rigorous methodology was established by utilizing numerical data sets from the closely related property, namely 17-4PH stainless steel. This approach ensures the experimental foundation is both technically consistent with established machining research practices, showcasing the accuracy of the algorithm.

3.2.1. Material Selection

The work material for this study is 15-5PH (Precipitation-hardening) stainless steel, chosen for its high strength and hardness coupled with good corrosion resistance, which makes it attractive for aerospace and high-performance applications. 15-5PH shares the same martensitic matrix and copper precipitate strengthening mechanism as 17-4PH, resulting in a comparable response to materials behaviour under load. However, direct cutting experiments on 15-5PH were not available for this research. To compensate, experimental machining parameters and material data were obtained from the literature on 17-4PH stainless steel, as shown on the Table 3.1. The Johnson-Cook constitutive constants and cutting conditions for 15-5PH, a well-documented alloy in machining research, were used as initial inputs to approximate the behavior of 17-4PH. This approximation is justified by the similar aging ability and strength levels of 17-4PH and 15-5PH; both alloys reach high yield strengths between 1180 and 1310 Megapascal (MPa) and hardness after a single-step aging in the 480 to 620 °C range [51]. This approach allowed the study to proceed with calibrating 15-5PH's material model despite the lack of direct empirical data, while maintaining the wellestablished reference of 17-4PH.

Parameters	A	В	n	m	С	T-Q
Values	1000	700	0.50	0.75	0.05	0.80

Table 3.1: Johnson-Cook parameter and Heat Infraction for 17-4PH Stainless Steel [51].

3.2.2. Cutting Parameters and Tool Geometry

The cutting tool used for this research is rigid, with a manufacturer's code of KPR95CTA6CLA7 for the tool. In this tool, the designation as shown in Figure 3.3, TA6C indicates a top rake angle of 6°, and LA7 indicates a clearance angle of 7° on the tool's flank. Also, Table 3.2 shows the features of the Cutting Tools for this study, which were extracted from MISULAB.

Symbol	Feature Name	Value	Unit
CLA	Clearance angle	7	0
CTA	Cutting angle	6	0
EDG	Edge length	15.504	mm
ESR	Edge sharpness radius	0.03	mm
AMG	Insert angle	55	0
REP	Insert tip radius	11	mm
KPR	Tool lead angle (KAPR)	95	0

Table 3.2: Features of The Cutting Tools and their Parameters.

Thus, the tool had a moderately sharp geometry typical for finish turning operations. This well-defined geometry with a known rake and clearance angle is important for accurate simulation, since the tool angles affect the stress and contact conditions at the chip-tool interface.

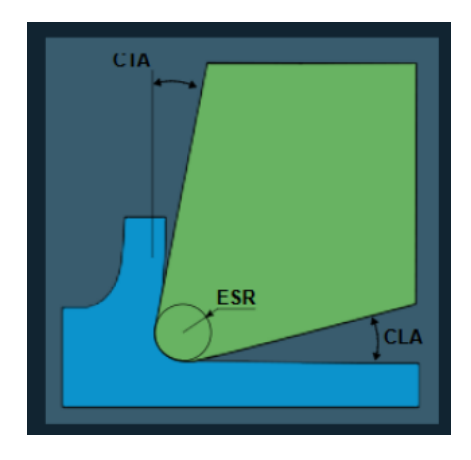


Figure 3.3: Orthogonal Cutting Tools

The cutting conditions for the speed and feed were selected based on machining parameters reported for similar PH stainless steels. A cutting speed of 120 m/min and a feed rate of 0.20 mm/rev were applied, falling in the mid-range of conditions used in prior 17-4PH and 15-5PH in this research study [52]. By extending this uncut chip thickness ranging from 0.10 to 0.25 mm, we obtained multiple reference cutting conditions for the inverse calibration. In practice, this meant that the experiments were run at several uncut chip thicknesses, ranging from 0.10 to 0.25 mm, while keeping speed and feed constant, allowing for the observation of several distinct chip formation regimes. Using a range of uncut chip thicknesses is important because it produces different chip morphology and force levels, thereby providing more data points to

constrain the material model. Indeed, previous researchers have shown that calibrating constitutive parameters over a design of experiments covering various cutting depths and speeds leads to robust parameter identification [53]. Following that approach, the inclusion of several depth-of-cut levels in our setup helps to extract multiple calibration points at different cutting stress states, which improves the reliability of the inverse modelling results.

3.3. Numerical Simulation with Abaqus

To investigate the machining conditions of 15-5PH stainless steel, finite element simulations were conducted using Abaqus under the same conditions as the experiments. The simulation model replicates orthogonal cutting in both two dimensions (2D) at different cut sections to three dimensions (3D), including the detailed geometry, mesh design, boundary conditions, frictional interactions, and the Johnson-Cook material constitutive behaviour. The following subsections describe the modelling methodology in detail, as part of the thesis methodology, to ensure clarity.

3.3.1. Uncut-Chip Thickness (H_{ref}) Computation

Uncut chip thickness (H_{ref}) is a critical parameter in turning operations that defines the thickness of the material layer being removed or deformed during the cutting operation. Computation of uncut chip thickness in the Misulab software is the critical step and needs more attention. In the Figure 3.4, as shown below, the cut section (CS) is divided into several 2D elementary orthogonal sections with an uncut chip thickness. The shape of this section CS depends on the cutting conditions (depth of cut ap, feed f) and the tool geometry (tool tip radius R). For the current case study, five intervals of reference uncut chip thickness, which are 0.10, 0.15, 0.175, 0.23, and 0.25mm were used as the cut section.

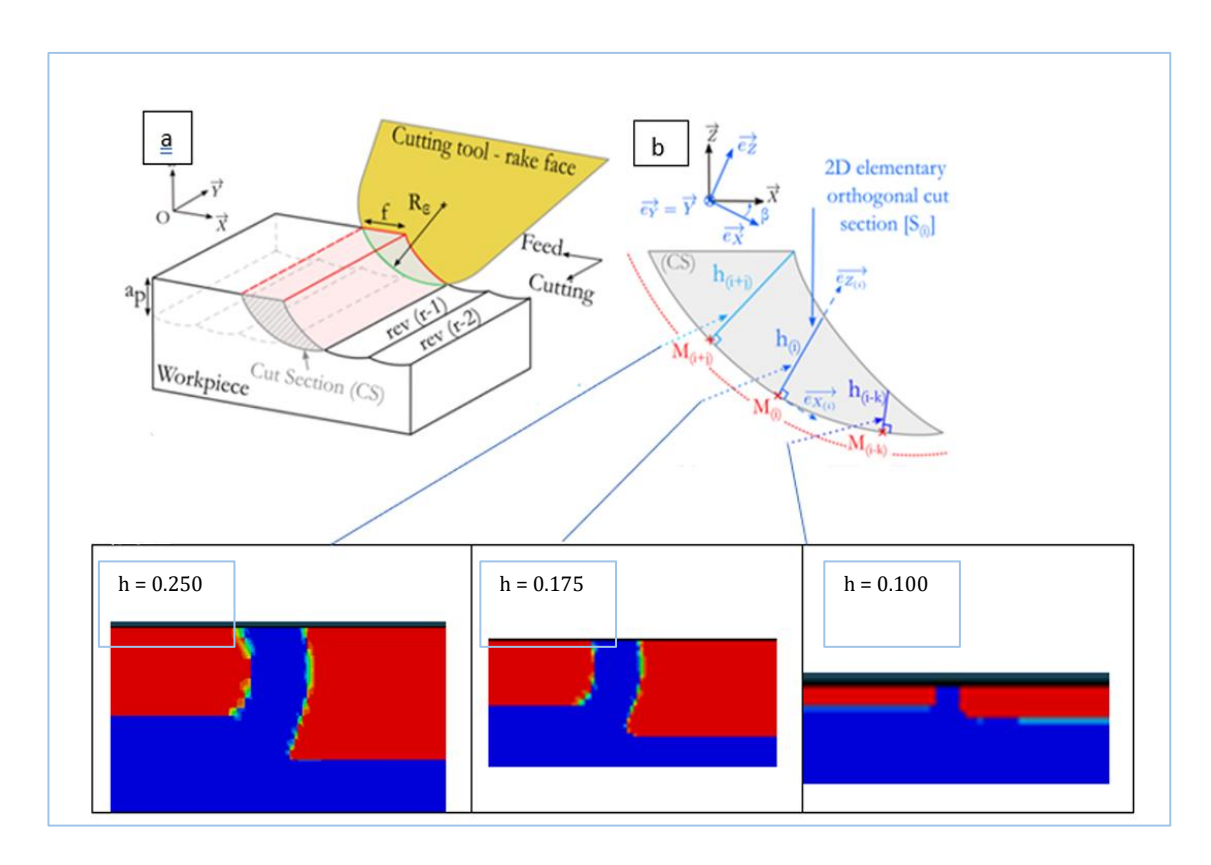


Figure 3.4: Schematic of the orthogonal cutting model. (a) 3D view of a turning operation and (b) the corresponding 2D plane strain cutting slice with uncut chip thickness H_{ref} . [54]

The 2D model represents a longitudinal section of the machining process under plane strain conditions. The workpiece is modelled as a rectangular domain, as illustrated in Figure 3.5 with dimensions large enough (several millimetres in length (L) and height (H)) to prevent boundary effects from influencing chip formation.. The 2D models accurately replicate the actual cutting insert geometry. For the workpiece, four-node plane strain elements (CPE4R) are used. The mesh is refined in critical regions: the primary shear zone and tool-chip interface, where strain and temperature gradients are highest. The smallest element size is set to $5\mu m$, ensuring that at least 10-20 elements are in the uncut chip thickness for sufficient resolution. To balance computational efficiency and accuracy, the mesh is partitioned into a fine zone near the cutting region and a coarser zone elsewhere.

The cutting tool is modelled as rigid with a sharp edge and assigned the exact rake and clearance angles from the experimental setup. Its surface mesh is designed to properly interact with the refined workpiece mesh. All material properties, including density, elastic modulus, thermal conductivity, and specific heat, are assigned based on 15-5PH steel data to maintain consistency with physical behaviour.

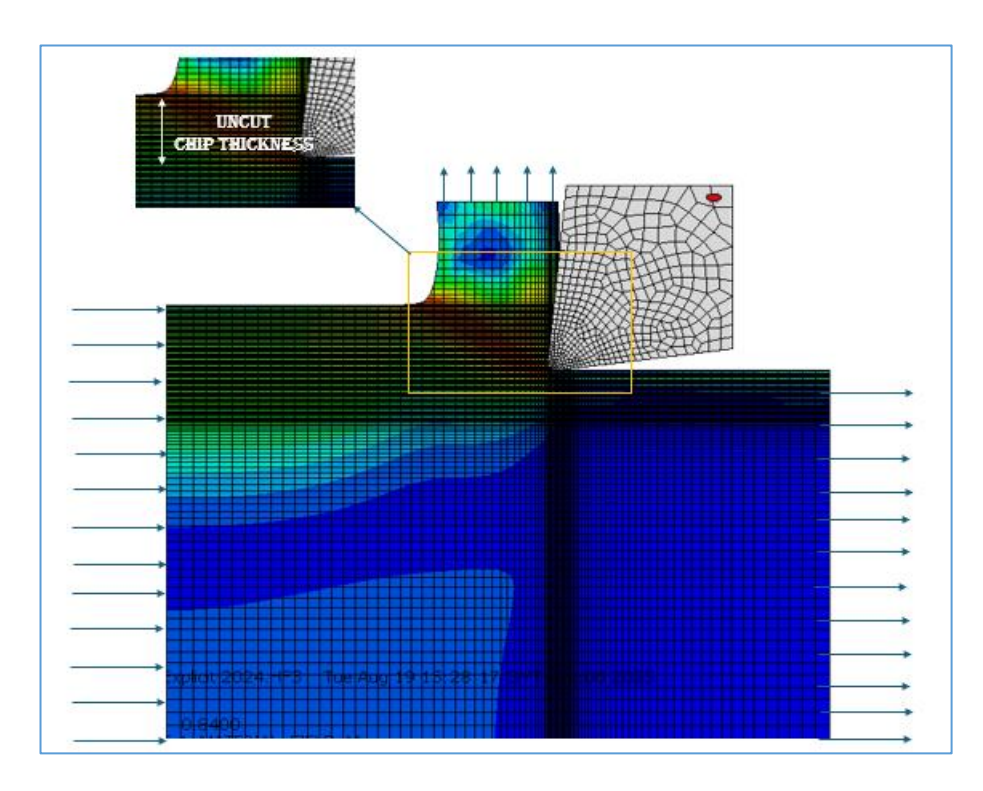


Figure 3.5 : Schematic of a 2D finite element model, showing the cutting depth, refine mesh and boundary conditions.

3.3.2. Boundary Conditions and Friction

The simulation setup employed fixed boundary conditions for the cutting tool while assigning a constant translational velocity of 2 mm/s to the workpiece along the cutting direction. This configuration maintained the experimental cutting speed equivalence while optimizing computational efficiency through mass scaling in the explicit dynamic analysis. The selected machining cutting speed was 120 m/min across all uncut chip thicknesses, preserving quasi-adiabatic conditions during chip formation while enabling practical simulation times.

Through iterative simulations, we observed that increasing the friction coefficient from the baseline μ = 0.279 to μ = 0.55 produced more physically realistic tool-chip contact behaviour. This adjustment resulted in:

- Extended contact length along the tool rake face
- Improved stress distribution matching experimental observations
- Enhanced thermal interaction at the interface

However, the Table 3.3 illustrates the parameters used for the Abaqus Explicit model for this research study in the properties of 15-5Ph stainless steel.

The contact interaction between the tool and workpiece is defined with frictional and

thermal properties, and a friction model governs the tangential behaviour. In this research, a Coulomb friction law with a constant coefficient of friction (μ) is used to model the tool-chip interface. Based on machining literature and stainless steel cutting best practices, μ was set in the range 0.3-0.5, and a value of $\mu \approx 0.3$ was used in the simulation model. This simple model assumes a sliding interface with a constant friction coefficient. This leads to a distribution of normal and shear stress along the rake face, with an initially high, near-constant shear stress (sticking) that drops off toward the edge of contact (sliding).

Category	Parameter	Value/Description
Workpiece Material	Johnson-Cook Model	A, B, n, C, m parameters
Tool Material	Elastic Modulus (E)	620 GPa
	Density (ρ)	14.6 g/cm^3
	Inelastic Heat fraction	Taylor-Quinney, $\beta = 0.6-0.95$
Contact Properties	Friction Coefficient (μ)	0.279, adjusted to 0.55
	Damping	3% critical damping
	Heat Partition	85% to workpiece
Simulation Settings	Analysis Type	Explicit dynamic
	Total Simulation Time	0.4sec in (Abaqus Software)
	Iteration Timing	8161.1sec in each Iteration

Table 3.3: Material Properties and Simulation Parameters for 15-5PH Stainless Steel Machining Model

At the tool-chip interface, thermal contact is also important. We enabled frictional heating such that a fraction of the plastic work done by friction is converted to heat. In Abaqus, by default, 85% of the frictional dissipated energy is converted to heat, and we assume this for maximum heating effect. Additionally, a high thermal conductance was defined for the contact to allow heat flow from the hot chip into the tool. The workpiece material's thermal properties were included so that temperature fields would evolve realistically. As a result of these settings, heat generation occurs from two sources during simulation: plastic deformation and friction along the tool rake face. The plastic deformation was assumed to convert to heat at a specified inelastic heat fraction (commonly 0.9, meaning 90% of plastic work converts to heat), which is standard for metals undergoing adiabatic deformation. Together, these thermal conditions ensure that the model predicts cutting temperature rise and thermal softening effects in the

chip formation process. However, the mechanical and thermal boundary conditions: the tool is fixed and thermally insulated, the workpiece is moving and adiabatic on free surfaces, and the tool-chip interface obeys Coulomb friction with frictional heating included.

3.3.3. Implementation of Johnson-Cook Parameters

To use this model in Abaqus Software, we input the five parameters (A, B, n, m, C) along with the Taylor-Quinney coefficient, the reference strain rate and the relevant temperature constants (melting temperature T_{melt} and reference ambient temperature). The simulations are fully coupled thermo-mechanical analyses, meaning that the deformation (stress/strain) and temperature evolution are solved together at each time increment. In our Abaqus material definition, we set $\dot{\epsilon}_0$ As $1s^{-1}$, so C directly scales the increase in flow stress per decade of strain-rate increase. The temperature-dependent term was implemented with T_{room} as 20°C and T_{melt} At 1440 °C, which attained the property of 15-5PH stainless steel, to properly normalize the homologous temperature in the J–C model. Table 3.4 below shows the Johnson-Cook parameter for 15-5PH, which was set as the reference initial parameter.

Initial	A	В	n	m	С	έ ₀	T_{melt}	T_{room}	T-Q
Parameters									
Values	855MPa	448MPa	0.14	0.63	0.0137	$1.0s^{-1}$	1440°c	20°_c}	0.70

Table 3.4: Johnson-Cook parameters and Taylor Quinney for 15-5 PH [39]

Since the experimental data for 15-5PH wasn't given, we used the Johnson-Cook Parameter of 17-4PH stainless steel, showing the machining condition, and then optimized it for 15-5PH to reach the 17-4PH machining condition. We used literature values of J-C parameters for 15-5PH as a first guess, as shown in Table 3.4 above. These initial values were further adjusted to account for 17-4PH's material behaviour parameter.

The Johnson-Cook parameters were implemented in Abaqus by editing the input file and via Python scripting to ensure consistency and automation in this research. A custom Python script was developed to automate the simulation workflow for inverse identification: it would read a set of J-C parameters, along property, modify the Abaqus .inp file accordingly updating the Material definition section with the new A, B, n, m, C

and Taylor-Quinney values, submit the job, and then extract results for cutting force, penetration force, chip thickness, and contact length from the output database (odb). This automation allowed running numerous simulations to search for the parameter set that best matches the experimental results. The script also ensured that each simulation had the same mesh, boundary conditions, and settings, varying only the material parameters, which is crucial for a fair comparison. The *inp* modifications included not only the material behaviour flow stress parameters but also the Equation of State for thermal coupling and Specific Heat to calculate temperature rise. Because Abaqus's built-in Johnson-Cook model was used, the coupling between strain rate and temperature is inherently handled: the instantaneous temperature is used in the material model at each increment to reduce the yield stress, and the current strain rate is used to increase it, achieving a realistic material behaviour parameter.

During the simulation, the cutting conditions were identical to those of the experiments: a cutting speed of 120 m/min, with uncut chip thicknesses ranging from 0.10mm for a "light cut" to 0.25mm for a heavier cut, and a feed of 0.2 mm/rev in the actual turning tests. The 3D model, on the other hand, simulates each cut segment of the uncut chip thickness. By keeping these conditions consistent, the simulation outcomes, cutting forces, and chip morphology can be directly compared to experimental measurements for validation and for the inverse identification of the J-C parameters.

The steady-state chip thickness from the simulation was then compared to the experimentally observed chip thickness. The cutting force F_c and penetration force F_p were obtained from the simulation by orientation of the reaction forces on the tool in the cutting direction and penetration direction, respectively. In Abaqus/Explicit, the contact forces on the rigid tool can be output; were will integrate this over time or take an average during the steady cutting phase to get a representative force value. The contact length along the tool rake face, the length of the tool in contact with the chip, was determined by examining which nodes/elements of the chip were in contact with the tool at steady state. That distance from the tool tip is the contact length. All these processing steps were done using either the Abaqus Visualization module or automated via script to ensure accuracy.

However, the numerical simulation in Abaqus software provided a virtual machining experiment under controlled conditions identical to the real cutting tests. The Johnson-Cook material model was implemented and calibrated for 15-5PH, allowing the simulation to predict how this material shears and softens at high strain rates and

temperatures. By matching the simulation to experimental cutting forces, chip geometry, and perhaps temperatures, the J-C parameters were inversely identified with accuracy. This detailed FE simulation methodology forms a core part of the research's approach, ensuring that the results are grounded in a rigorously developed model. The algorithm was run iteratively, and the processing of outputs like chip thickness, forces, and contact length enabled direct comparison to experiment, thereby validating the model and supporting the material parameter identification.

3.4. Python-Abaqus Coupling

In this research, a Python scripting interface is coupled with Abaqus finite element simulations to automate the simulation-optimization loop. Python scripts modify Abaqus input files (.inp), submit analysis jobs, and then parse Abaqus output database files (.odb) to extract results of interest. This integration allows iterative refinement of material parameters-specifically the Johnson-Cook constitutive parameters and the Taylor-Quinney coefficient-based on comparisons between simulation outputs and experimental measurements. The following subsections detail the data extraction process and the overall automation workflow.

3.4.1. ODB Data Extraction

Abaqus stores simulation results in an output database file (.odb). Using the Abaqus Python scripting API, the developed script opens each .odb after a run and programmatically retrieves the machining outcome needed for calibration. In particular, the script queries the output database for: chip geometry, tool-chip contact length, and the forces. These quantities may be obtained from field output data or history output probes defined in the model. For example, the chip thickness can be determined from nodal displacement/coordinate data measuring the thickness of the formed chip at steady-state, while the contact length can be extracted from the contact status along the tool-chip interface. The cutting and penetration forces are obtained from reaction force outputs on the tool in the cutting direction and penetration direction, respectively. The Python script uses Abaqus Scripting Interface commands to access such results from the *odb* without manual intervention. The extracted values are written to an output text file for further processing. This automated extraction is crucial for the iterative optimization. it enables the loop to evaluate the simulation *vs.* experiment discrepancy after each run. As a sample, the script can launch an Abaqus

job for a given input file and, upon completion, directly open the resulting *odb*, read specified node or element outputs, and save these results. By automating the processing in this manner, the methodology ensures that the key machining condition indicators are consistently obtained from each simulation run for comparison with experimental values.

3.4.2. Automation Workflow

The process of the Python workflows begins with an initial guess of J-C material parameters and TQ coefficient, then cycles through simulation, error evaluation, sensitivity analysis, and parameter update (via Levenberg-Marquardt) until convergence. Figure 3.6 showcases a Flowchart illustrating the Python-ABAQUS coupled simulation and optimization workflow.

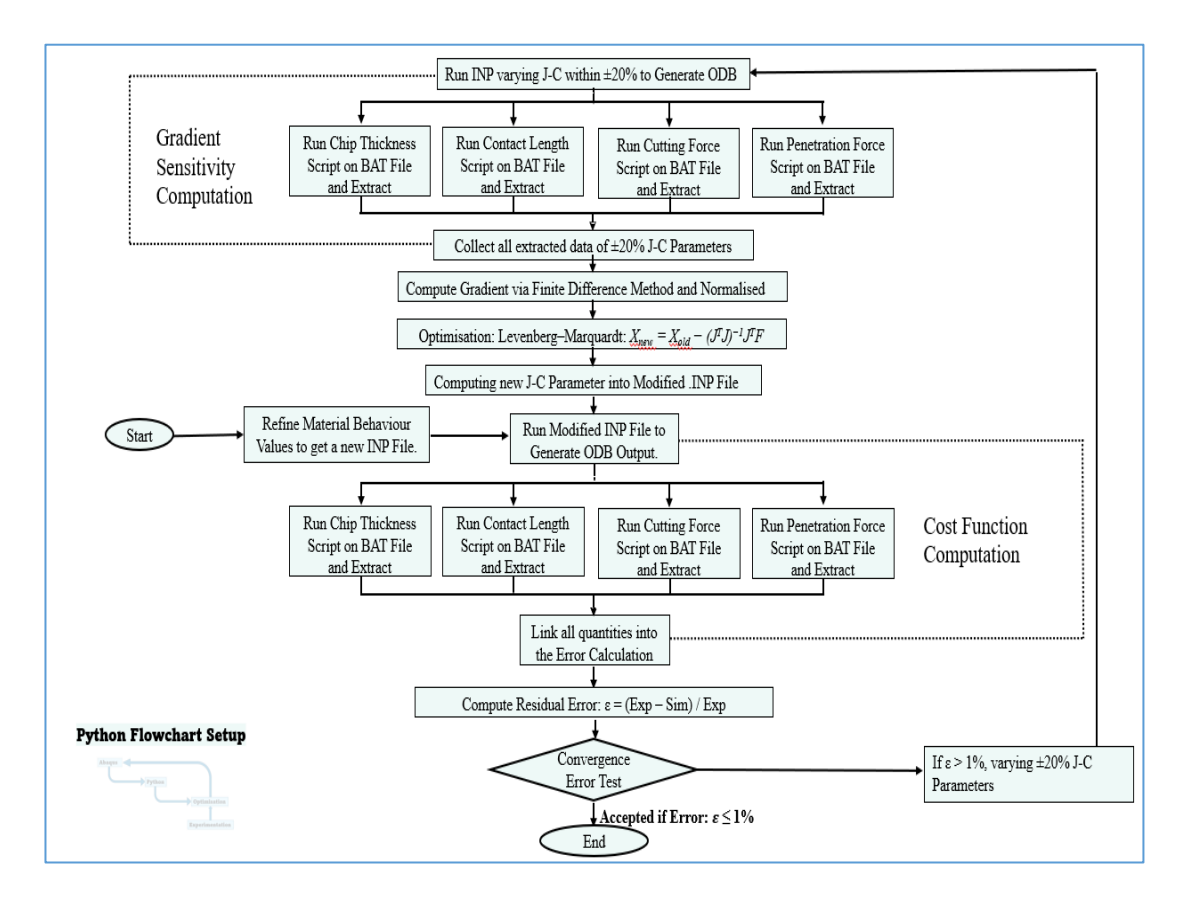


Figure 3.6: The inverse algorithm flowchart was adopted for the identification of the material behaviour parameter on the Python interface.

The overall automated workflow in the Figure 3.6 above proceeds as follows. First, an initial set of J-C parameters (Reference Johnson-Cook Parameters of 15-5PH Stainless

Steel) and the Taylor-Quinney coefficient is assumed. These values are embedded in the Abaqus input file; for instance, the material definition in the .inp file is updated with a Plasticity line for the Johnson-Cook model and an Inelastic Heat Fraction for the TQ coefficient. This ensures the FE model uses the current parameter values for material behaviour. The Python script automates the editing of the input file and then utilizes Abaqus to run the simulation (e.g., via a command like 'abaqus job file in the inp'). Once the simulation completes, the script extracts the resulting chip thickness, contact length, cutting force, and penetration force from the .odb as described in Figure 3.6. These simulation outputs are then compared to the experimentally measured values for the same machining conditions. Firstly, before Optimisation begins, a convergence criterion is evaluated using the residual error in each output, as shown in Eq. (3.1), while for Eq. (3.2) is for the Residual Error for all Machining Output.

Residual Error for Each Machining Output:
$$\varepsilon_i = \frac{E_i^{exp} - E_i^{sim}}{E_i^{exp}}$$
 (3.1)

Residual Error for all Machining Ouput:
$$\frac{1}{100} \sum_{i=1}^{4} \varepsilon_i^2 = \frac{1}{100} \sum_{i=1}^{4} \left(\frac{E_i^{exp} - E_i^{sim}}{E_i^{exp}} \right)^2$$
 (3.2)

Where; E_i^{exp} : the experimental value. E_i^{sim} : the simulation result for that metric.

This relative error indicates how far the simulation is from reality (Experimental Machining). If the magnitude of ε_i If all key outputs are within an acceptable tolerance,

calibrated. When calibration has not yet converged, the Python-Abaqus coupling enters

it should be $max_i\%\varepsilon_i \leq 2\%$. Then, if not, the current parameters are considered

an iterative loop to update the material parameters using a Levenberg–Marquardt (LM) optimization algorithm.

The optimisation algorithm starts with the Gradient Sensitivity Computation, where the influence of each material parameter on each output is quantified via a gradient-based sensitivity analysis. The script perturbs each Johnson-Cook and Taylor-Quinney parameter with $\Delta X_i = \alpha X_i$, By a small amount (using a symmetric percentage of $\alpha = 0.20$ of the current value, X_i) and runs additional Abaqus simulations for each perturbation. For each parameter, it was either conducted to run in the range of with ΔX_i increased i.e. $1.2\Delta X_i$ to the decrease range of ΔX_i i.e. $0.8\Delta_{pj}$ which is ± 0.20 range, while keeping all other parameters at their current values. From these perturbation simulations, the changes in outputs are recorded. A forward finite difference

approximation is shown in Eq. (3.3) is then used to estimate the partial derivative of each output. F_i for parameter ΔX_i :

$$\frac{\partial F}{\partial X_i} = \frac{F(X_i + \Delta X_i) - F(X_i)}{\Delta X_i} \tag{3.3}$$

Where; $\Delta X_i = \alpha X_i (\alpha = 0.20)$: ±20% of the base J-C parameter value $F(X_i \pm \Delta X_i)$ =Perturbation Outputs Values $F(X_i)$ = Baseline Outputs Values

These derivatives form a Jacobian (sensitivity) matrix, which is; $J \in \mathbb{R}^{m*n}$ Of m and n (here m=4outputs and n=6parameters) as shown in Eq. (3.4) By construction, the (i.j) entry of J is the sensitivity of output I, where I are the chip thickness, contact length, cutting force, and penetration force, Also concerning parameter J as β , A, B, n, m, or C.

$$J_{i} = \begin{vmatrix} \frac{\partial F_{1}}{\partial T_{Q}} & \frac{\partial F_{1}}{\partial A} & \frac{\partial F_{1}}{\partial B} & \frac{\partial F_{1}}{\partial n} & \frac{\partial F_{1}}{\partial m} & \frac{\partial F_{1}}{\partial C} \\ \frac{\partial F_{2}}{\partial T_{Q}} & \frac{\partial F_{2}}{\partial A} & \frac{\partial F_{2}}{\partial B} & \frac{\partial F_{2}}{\partial n} & \frac{\partial F_{2}}{\partial m} & \frac{\partial F_{2}}{\partial C} \\ \frac{\partial F_{3}}{\partial T_{Q}} & \frac{\partial F_{3}}{\partial A} & \frac{\partial F_{3}}{\partial B} & \frac{\partial F_{3}}{\partial n} & \frac{\partial F_{3}}{\partial m} & \frac{\partial F_{3}}{\partial C} \\ \frac{\partial F_{4}}{\partial T_{Q}} & \frac{\partial F_{4}}{\partial A} & \frac{\partial F_{4}}{\partial B} & \frac{\partial F_{4}}{\partial n} & \frac{\partial F_{4}}{\partial m} & \frac{\partial F_{4}}{\partial C} \end{vmatrix}$$

$$(3.4)$$

Given the disparate matrix and magnitudes of outputs and parameters, we normalize the sensitivities for meaningful comparison. A normalized sensitivity matrix in Eq. (3.5)

$$J_{ij} = \frac{X_i}{F_i} \frac{\partial F_i}{\partial_{X_i}} \tag{3.5}$$

It is formulated by scaling the partial derivatives to a normalised sensitivity matrix in Eq. (3.6);

$$J_{ij} = \begin{vmatrix} \frac{\partial F_{1}}{\partial T_{Q}} \frac{T_{Q}}{F_{1}} & \frac{\partial F_{1}}{\partial A} \frac{A}{F_{1}} & \frac{\partial F_{1}}{\partial B} \frac{B}{F_{1}} & \frac{\partial F_{1}}{\partial n} \frac{n}{F_{1}} & \frac{\partial F_{1}}{\partial m} \frac{n}{F_{1}} & \frac{\partial F_{1}}{\partial C} \frac{C}{F_{1}} \\ \frac{\partial F_{2}}{\partial T_{Q}} \frac{T_{Q}}{F_{2}} & \frac{\partial F_{2}}{\partial A} \frac{A}{F_{2}} & \frac{\partial F_{2}}{\partial B} \frac{B}{F_{2}} & \frac{\partial F_{2}}{\partial n} \frac{n}{F_{2}} & \frac{\partial F_{2}}{\partial m} \frac{n}{F_{2}} & \frac{\partial F_{2}}{\partial C} \frac{C}{F_{2}} \\ \frac{\partial F_{3}}{\partial T_{Q}} \frac{T_{Q}}{F_{3}} & \frac{\partial F_{3}}{\partial A} \frac{A}{F_{3}} & \frac{\partial F_{3}}{\partial B} \frac{B}{F_{3}} & \frac{\partial F_{3}}{\partial n} \frac{n}{F_{3}} & \frac{\partial F_{3}}{\partial m} \frac{n}{F_{3}} & \frac{\partial F_{3}}{\partial C} \frac{C}{F_{3}} \\ \frac{\partial F_{4}}{\partial T_{Q}} \frac{T_{Q}}{F_{4}} & \frac{\partial F_{4}}{\partial A} \frac{A}{F_{4}} & \frac{\partial F_{4}}{\partial B} \frac{B}{F_{4}} & \frac{\partial F_{4}}{\partial n} \frac{n}{F_{4}} & \frac{\partial F_{4}}{\partial m} \frac{n}{F_{4}} & \frac{\partial F_{4}}{\partial C} \frac{C}{F_{4}} \end{vmatrix}$$

$$(3.6)$$

Each derivative for the parameters; ∂_{X_i} represents the fractional change in output ∂F_1 caused by a fractional change in the parameter X_i . This normalization facilitates assessing which parameters have the most pronounced effect on each output. The sensitivity analysis thus identifies the most and least influential parameters and provides the local gradient needed for the optimization algorithm. [55].

Then, for the Parameter Update via Levenberg-Marquardt, with the normalised sensitivity matrix J Computed, the algorithm updates the parameter set of $[\beta, A, B, n, m, C]$ to reduce the output error. We define a cost function of r_i which will be used in Eq. (3.7) as;

$$r_i = E_i^{exp} - E_i^{sim} (3.7)$$

As the sum of residuals between simulation outputs and experiments. For all four target outputs, the cost is shown in Eq. (3.8).

$$E = \sum_{i=1}^{4} r_i = \sum_{i=1}^{4} (E_i^{exp} - E_i^{sim})$$
 (3.8)

The goal is to find the parameter adjustment of the materials' behaviour that minimizes the machining outputs. A Newton-Raphson or Gauss-Newton approach would solve $J=\frac{\partial r}{\partial p}$ where J is the Hessian matrix of second derivatives to update the parameters. Here, we adopt the Levenberg-Marquardt (LM) algorithm as shown in Eq. (3.9), and Eq. (3.10), which is a robust variant of Gauss-Newton, to perform the update. The LM method is well-suited for non-linear least squares problems and is more robust than plain Gauss-Newton in many cases. It works by blending Gauss-Newton steps with gradient-descent steps, controlled by a damping factor λ . Specifically, LM uses the Jacobian, J, to approximate the Hessian as H, which is J^TJ (the Gauss-Newton approximation) and computes the parameter correction by solving the modified normal equations in the Eq. (3.10).

$$(J^T J + \lambda)\Delta_P = J^T r \tag{3.9}$$

$$\Delta_p = -(J^T J + \lambda)^{-1} J^T r \tag{3.10}$$

Here r Is the vector of output errors. By adding λ (a scaled identity matrix) To the Hessian approximation, the algorithm damps the update step. The value of λ is place at 10^{-2} . This adaptive damping gives Levenberg-Marquardt optimisation to improve stability compared to a standard Newton method, especially if the initial guess is far from the optimum or if J^TJ . Also, to keep the optimized parameters physically meaningful for martensitic precipitation-hardening stainless steels, a boundary limit is imposed so that the Johnson-Cook constant or the Taylor-Quinney coefficient cannot drift outside the range value of the property for martensitic steel. The limits were compiled from alloys with closely similar material behaviour property to 15-5PH—17-4PH, PH13-8Mo, and Custom 465, as shown in Table 3.5 and applied after each Levenberg-Marquardt update as a simple box-projection. [56]

Set Parameter	T-Q	A	В	n	m	С
Lower	0.60	400	100	0.05	0.5	0.005
Upper	0.95	1100	800	0.8	0.9	0.900

Table 3.5: Boundary Limit for the 15-5PH Stainless Steel. [56]

Thus, the trial update for a new set of parameters is optimised between lower and upper bounds according to Eq. (3.11).

$$P_{new} = min(max(P_{old} + \Delta_P, P_{lower}), P_{upper})$$
(3.11)

The theory for this parameter estimation approach is based on the deterministic Levenberg–Marquardt algorithm as described by Guyon and Le Riche, where sensitivities and a modified Hessian are used to iteratively refine model parameters in a least-squares sense. The updated parameter vector, which is shown in Eq. (3.12).

$$P_{new} = P_{old} + \Delta_P \tag{3.12}$$

Where; P_{new} Is the new set of Johnson-Cook Parameters and Taylor-Quinney Cofficient P_{old} Is the previous set of Johnson-Cook Parameters and Taylor-Quinney Cofficient

This is then written back into the Abaqus input file, replacing the old Johnson-Cook Parameters and Taylor-Quinney values. The Python script then launches a new Abaqus simulation with the modified input and again performs ODB extraction of chip thickness, forces, etc. The new simulation outputs are compared to experiments, yielding new residual errors. r_i . The convergence test is repeated: if all errors are now within tolerance, the optimization stops; if not, another iteration (sensitivity analysis + LM update) is executed. In this manner, the loop continues until either convergence is achieved or a maximum number of iterations is reached.

3.5. 2D and 3D Simulation Optimisation Workflow

With a robust inverse identification procedure in place, the simulation workflow proceeds in two stages: a 2D calibration stage followed by a 3D validation stage. This two-tier approach leverages the strengths of simple 2D models for efficient parameter tuning and then confirms the material model's performance in a more realistic 3D cutting scenario. The overall goal is to ensure that the identified constitutive parameters not only fit the 2D orthogonal cutting data but also generalize to true 3D machining conditions representative of industrial applications.

3.5.1. 2D Calibration Stage (Orthogonal Cutting in Plane Strain)

In the first stage, an orthogonal cutting simulation is performed in two dimensions. The workpiece is modelled as a rectangular plane, and the cutting process is simulated as a cross-sectional slice of a continuous chip formation. This 2D model captures the primary shear plane and tool-chip interface physics while assuming the width of cut is effectively infinite (no edge effects), which is a reasonable approximation for testing constitutive response in a controlled way. The advantage of the 2D FE model is its computational efficiency and stability; it involves far fewer elements than a full 3D model and thus runs faster, enabling the iterative optimization loop described in Section 3.4 to be executed in a feasible time. Using the 2D simulation, the Johnson-Cook parameters and the Taylor-Quinney heat coefficient are calibrated by minimizing the error between simulated and measured chip thickness, contact length, cutting force, and penetration force. The Python-driven loop automatically updates the material definition and reruns the 2D simulation until convergence criteria are met, yielding a parameter set that closely reproduces the experimental cutting data in the 2D orthogonal cut model. Throughout this stage, the cutting conditions (cutting speed,

uncut chip thickness, tool geometry, friction, etc.) are matched to the experiments. For instance, if the experiments were at 120 m/min with an uncut chip thickness of 0.20 mm, the 2D simulation uses the same conditions. By the end of the 2D calibration stage, we obtain a tuned material model that provides an excellent fit in an idealized orthogonal cutting scenario.

3.5.2. 3D Validation Stage for the Full 3D Machining Simulation

To move from 2D to 3D integration is cast as a single multi-condition inverse problem that yields one calibrated parameter vector for all simulations. All 2D orthogonal-cut cases are fused by stacking a 12-output bundle composed of exactly: one deformed chip thickness, one tool-chip contact length, five cutting forces (from five H_{ref} conditions), and five penetration forces (the same five H_{ref} conditions). Using this bundle, a normalized residual vector is formed by comparing each simulated observable to its experimental counterpart. Local sensitivities are then computed by forward finite differences, perturbing each parameter for Taylor-Quinney, β , and the Johnson-Cook set A, B, n, C, m by ±20% while holding the others fixed. This yields a 12×6 Jacobian that feeds the Levenberg-Marquardt update. The cost function is the weighted sum of squared normalized residuals across the 12 outputs; the parameter increment solves the damped normal equations as shown in Eq. (3.13).

$$(J^T W^T W J + \lambda I) \Delta p = J^T W^T W r \tag{3.13}$$

Iterations continue until every element of the 12-component residual meets the convergence tolerances defined earlier. With a single best-fit coefficient set $\Delta p = [\beta, A, B, n, C, m]$ identified from the fused 2D problem, the model is lifted to 3D without re-tuning the material law. The validated 2D orthogonal configuration is extruded to 3D (same rake/clearance, friction, Taylor–Quinney setting, and tool-fixed/workpiecemoving kinematics), and the same 12-output bundle is regenerated: one chip thickness, one contact length, five cutting forces, and five penetration forces across the five H_{ref} cases. Here, it is a complex multiscale condition 2D fusion to obtain one physically consistent β + Johnson-Cook set, followed by direct reuse in 3D-demonstrates that the calibration generalizes from 2D to 3D machining predictions without post-hoc parameter tweaking.

Chapter 4 Results and Discussion

The results and discussion present a comprehensive analysis of the results obtained from the coupled Python-Abaqus, along with the Levenberg-Marquardt optimization workflow. The approach described in Chapter 3 was implemented to calibrate the Johnson-Cook (J-C) material parameters and the Taylor-Quinney (TQ) heat conversion coefficient for 15-5PH martensitic precipitation-hardening stainless steel under orthogonal cutting conditions. It is pertinent to note that, in the absence of machining experimental data for 15-5PH, the calibration was performed against experimental data for 17-4PH stainless steel numerical data to validate the optimized model. The 17-4PH stainless steel is a material with closely related martensitic precipitation-hardening characteristics. The primary objective of this chapter is to evaluate how accurately the calibrated model replicates this experimental machining behaviour across varying undeformed chip thicknesses (H_{refs}) and to discuss the physical implications of the results for machining mechanics and predictive modelling. Figure 4.1 illustrates the numerical simulation results for each H_{ref} case, showing the chip formation, stress distribution, and temperature fields obtained from the optimized parameter set.

The experimental data for 17-4PH showed a consistent increase in chip thickness, cutting force, and penetration force from the lightest cut section (0.10 mm H_{ref}) to the heaviest (0.25 mm H_{ref}), a trend that the numerical simulation successfully captures, as shown comprehensively in Figure 4.1. Observation trend for the tool-chip contact length, which increased from 0.10 mm to 0.150 mm, 0.175 mm, and 0.230 mm H_{ref} , before showing a slight reduction for the last cut section of 0.250mm H_{ref} .

The results follow a structured approach. First, the performance of the reference material parameter set is compared with experimental results to show the initial deviations. This serves as a baseline to understand the limitations of using uncalibrated parameters in high-strain-rate machining simulations. Next, the results from the optimized parameter set derived from the automated optimization loop are evaluated with experimental results in detail. The result discussion addresses key machining outputs, namely chip thickness, tool-chip contact length, cutting force, and penetration force, across five H_{ref} conditions (0.10 mm, 0.15 mm, 0.175 mm, 0.23 mm, and 0.25 mm). The analysis also includes an examination of error convergence trends and the stability of the optimization loop, providing a clear view into both the numerical

modelling and the physical reliability of the identified parameters.

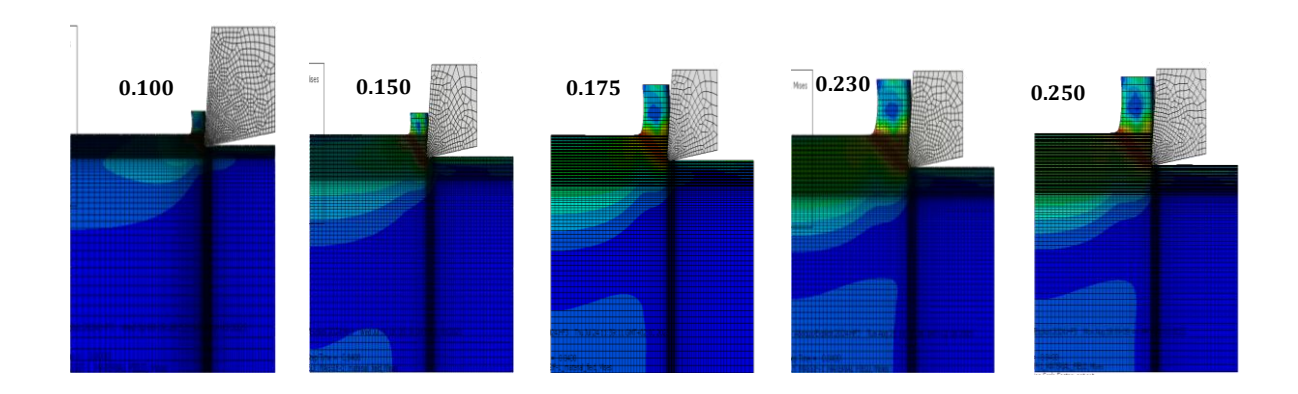


Figure 4.1: Numerical simulation results showing chip geometry, workpiece, and tool for each H_{ref} case

The results are interpreted not only quantitatively, using residual error metrics and graphical comparisons, but also physically, with an emphasis on the thermal-mechanical phenomena underpinning the observed machining responses. In doing so, the research shows how parameter calibration enhances the predictive result of the model, enabling accurate simulations that are suitable for both 2D orthogonal cutting and the extension to 3D process simulations in future studies.

4.1. Comparison of Experimental and Simulated Results Across H_{ref} Cases

This section opens the results-and-discussion chapter by putting the experiments side-by-side with two simulation states:

- The reference Johnson–Cook/Taylor–Quinney set used to seed the loop.
- The optimized set produced by the Python–Abaqus, along with the Levenberg–Marquardt routine.
- The five undeformed chip thickness levels were evaluated.

For each H_{ref} , we compare four observables that capture the core physics of cutting: chip thickness, tool–chip contact length, cutting (tangential) force, and penetration (thrust) force. Across all cases, the reference model shows typically from 20–40% on geometry and 28–40% on forces, while the optimized model

brought those differences to sub-percent for chip thickness and both force components less than 1%, and to 4.35% for contact length. Error-reduction traces show fast, monotonic convergence in ≤ 5 iterations for every H_{ref} ; the most optimised match occurs at 0.10mm H_{ref} , i.e., residuals fall from 74.35% to 0.053%, and the least optimised was 0.25mm H_{ref} , which is around 4.77%, which is still acceptable given the stronger thermal/friction non-linearities at the highest feed.

4.1.1. Chip Thickness

Experimentally, chip thickness increases monotonically with H_{ref} from about 0.185 mm at 0.10mm H_{ref} to roughly 0.436 mm at 0.25mm H_{ref} as shown in Figure 4.2. This shows stronger plastic compression as the undeformed chip thickness grows. This metric condenses the combined influence of strain, strain rate, and temperature in the primary shear zone, so it is a sensitive indicator of whether the constitutive law and heat conversion are realistic. With reference parameters, the model over-compresses the chip by an average of 21.94% across all H_{ref} between the Reference set and Experimental values. After optimisation, the model across all H_{refs} at an average drops to 0.49%, and the optimised curve collapses onto the experimental points at all five H_{refs} . Physically, that means the updated set of the Johnson Cook and Taylor-Quinney coefficient is producing the right effective flow stress over the actual strain–rate–temperature effect, so the shear plane angle and chip compression ratio are being predicted correctly. This fully shows that on-chip thickness is important, it also shows the thermal softening of the J-C Parameters and the inelastic heat fraction of the Taylor-Quinney now balance plastic work and heat generation such that the steady chip forms at the correct geometry.

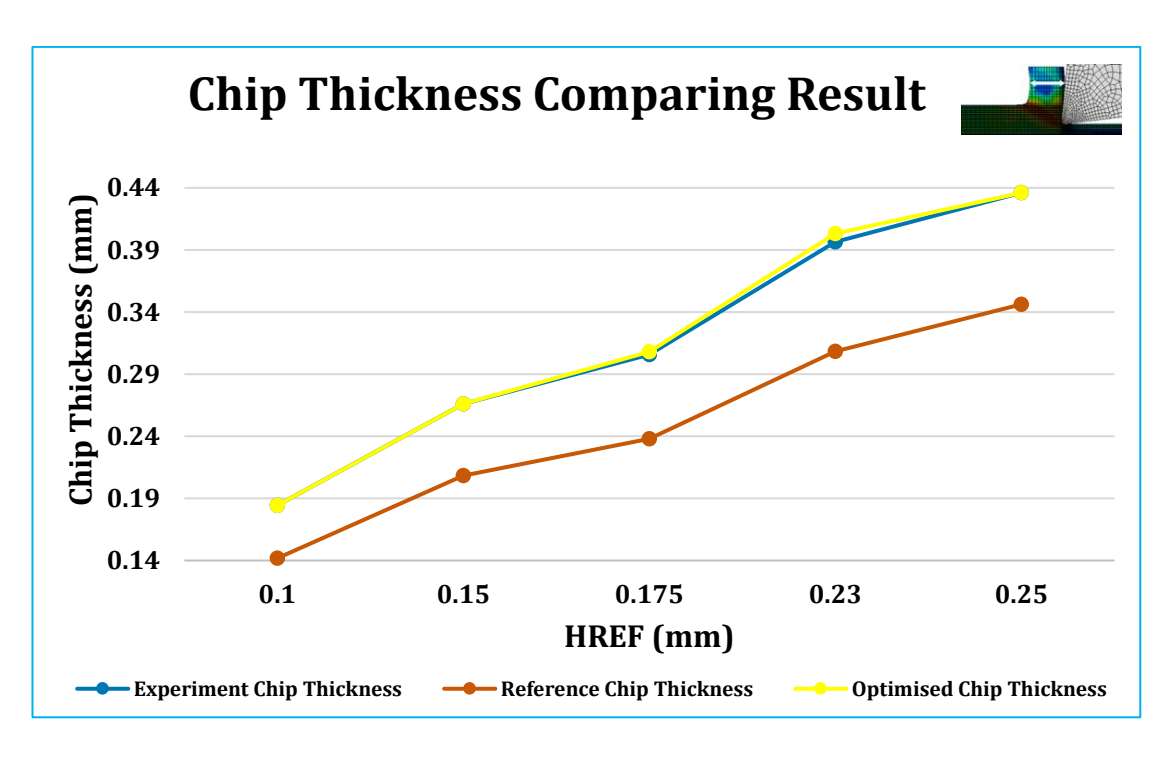


Figure 4.2 : Chip thickness against H_{ref} for both Experiment, Reference, and Optimisation.

4.1.2. Contact Length

The measured tool–chip contact length increases from 0.077 mm at 0.10 mm H_{ref} to approximately 0.314 mm at 0.23 mm H_{ref} , before slightly dropping to 0.297 mm at 0.25 mm H_{ref} . This mild non-monotonic behaviour at the highest feed is physically reasonable. As the undeformed chip thickness grows, the load and temperature along the tool–chip interface rise, modifying the frictional regime on the rake face. This shifts the balance between sticking and sliding zones and can shorten the effective sticking zone despite thicker chips.

Contact length is highly sensitive to interface physics, including pressure- and temperature-dependent friction and heat partition, as well as bulk material flow stress. Consequently, it often shows the largest prediction error when using a simplified constant-friction model. In this study, the reference simulation showed a deviation of about 41.20% across all H_{ref} cases. After optimisation, the error dropped to approximately 4.35%, indicating that the updated Johnson-Cook and Taylor-Quinney parameters refined the pressure-temperature distribution in the deformation zones and improved the predicted sticking-zone length.

The remaining small error at the 0.25mm H_{ref} is attributed to:

- The simplified friction model in the 2D orthogonal simulations.
- The absence of tool edge or nose radius effects present in real cutting operations.
- The high sensitivity of contact length to thermal partitioning at higher feeds.

The Figure 4.3 shows the trends of the Tool-Chip Contact length across all H_{ref} , where it shows in a plot of both the experiment, optimised and reference value residual errors.

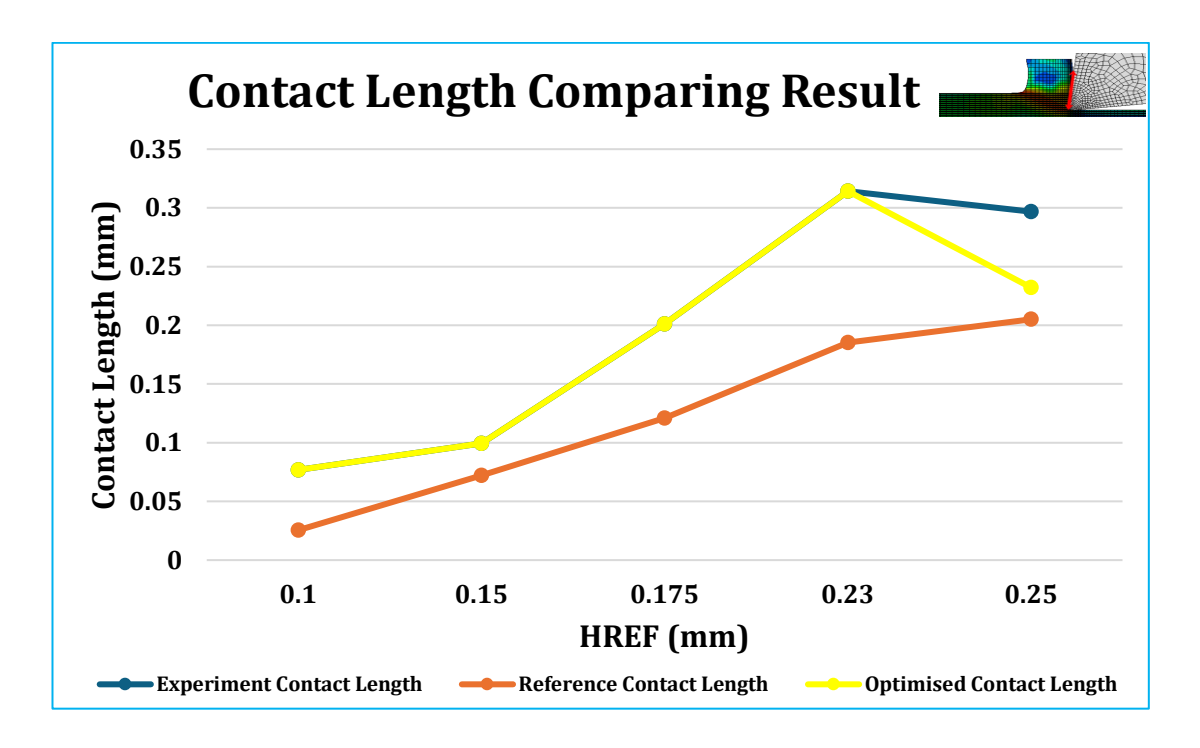


Figure 4.3: Contact Length against H_{ref} for both Experiment, Reference, and Optimisation.

4.1.3. Cutting Force (Tangential)

The tangential cutting force exhibits a steady and predictable increase as the undeformed chip thickness (H_{ref}) rises from 0.10 mm to 0.25 mm. At the lightest cut section (0.10 mm H_{ref}), the experimental cutting force is approximately 297 N, and this value escalates to around 672 N at the heaviest cut section (0.25 mm H_{ref}). This upward trend directly shows the increase in the engaged material area and the corresponding rise in the average shear stress developed in the primary deformation zone during the cutting process.

Under the reference Johnson-Cook and Taylor-Quinney parameter set, a significant deviation from the experimental measurements is observed, with an average error of approximately 40.21% across all H_{ref} levels. After applying the Python-Abaqus-LM optimisation loop, the tangential cutting force predictions show a remarkable optimisation improvement. The residual error reduces sharply to 0.34%, and the slope of the optimised cutting force across all H_{ref} curve aligns almost perfectly with the experimental results across all five cutting conditions. This level of agreement demonstrates that the optimised parameters accurately capture the mechanics of the primary shear zone, ensuring that the numerical model reproduces the stress-strain response of the material under dynamic conditions as shown in Figure 4.4.

From a physical perspective, the improved agreement indicates that the optimised Johnson–Cook parameters (A, B, n) successfully capture the static strength and strain-hardening characteristics, while the parameters (C, m) effectively model the strain-rate sensitivity and thermal softening effects in the cutting regime. Additionally, the inclusion of the Taylor-Quinney coefficient (β) ensures a realistic partitioning of plastic work into heat, which is critical for balancing the thermal–mechanical state within the primary shear zone. This balance is evident in the accurate force predictions, confirming that the model not only replicates the magnitude of the forces but also their underlying energy distribution mechanisms.

However, Such accuracy is particularly valuable for predictive simulations, enabling the calibrated model to serve as a reliable foundation for more complex 3D cutting simulations and digital twin applications, where precision in force prediction is essential for process planning, tool design, and performance optimisation.

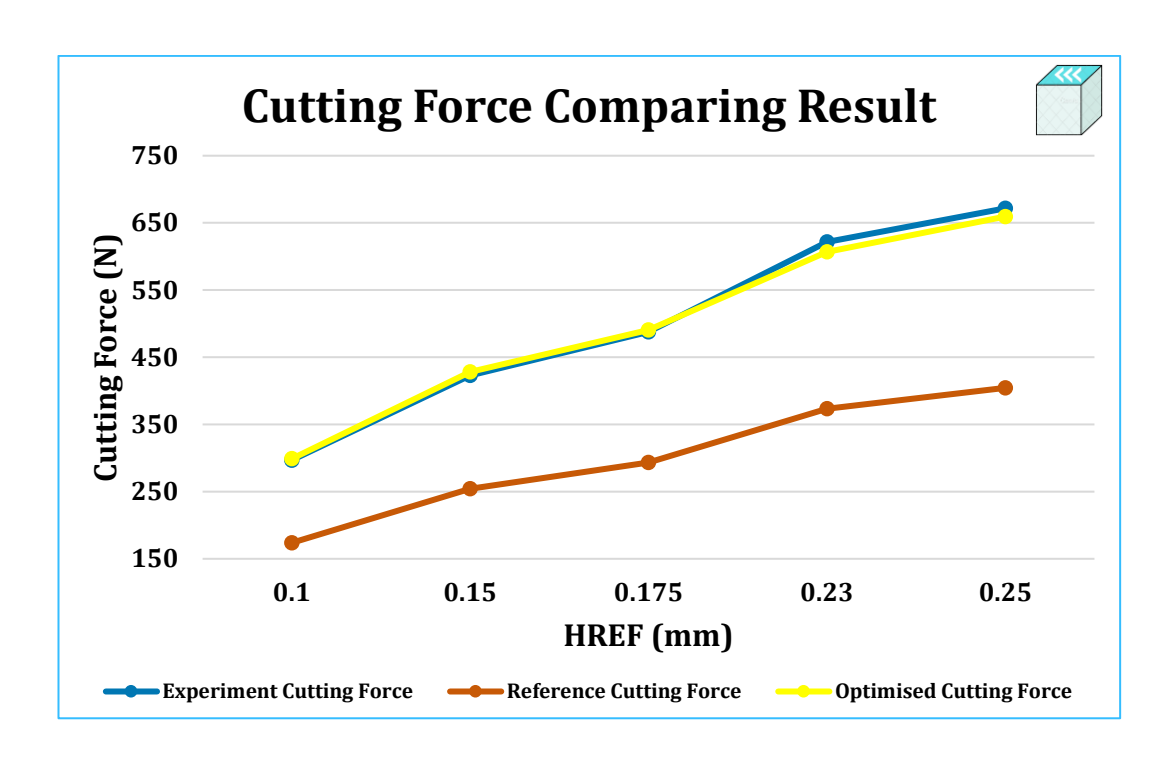


Figure 4.4: Cutting Force against H_{ref} for both Experiment, Reference, and Optimisation.

4.1.4. Penetration Force (Thrust)

The penetration force, often referred to as the thrust force, shows a progressive increase with undeformed chip thickness (H_{ref}), consistent with experimental observations. At the lowest H_{ref} of 0.10 mm, the measured thrust force is approximately 122 N, while at the highest H_{ref} of 0.25 mm, it rises to around 204 N. This trend is expected and aligns with fundamental cutting mechanics, as higher chip loads translate into greater normal pressures acting on both the rake and flank faces of the tool.

Physically, the thrust force reflects the interaction between chip flow angle, local pressure distribution, and thermal–mechanical effects at the tool–chip and tool—workpiece interfaces. It captures how chip formation and secondary deformation influence the directional partitioning of loads during the cutting process. Under the reference Johnson-Cook and Taylor-Quinney parameter set, a noticeable optimisation is observed, with an average deviation of approximately 28.37% across all H_{ref} conditions. Following the Levenberg–Marquardt-based optimisation loop, the error was drastically optimised to 0.14%. This significant improvement confirms that the optimised

parameter set not only captures the magnitude of the penetration force but also accurately reproduces the directional balance between tangential and normal components of the cutting forces. Such accuracy demonstrates that the chip flow kinematics and local stress distributions predicted by the finite element simulations are consistent with the actual machining behaviour.

From a practical perspective, achieving this level of agreement is crucial. It enables more reliable predictions for tool loading, tool deflection, and surface integrity trends, particularly under severe plastic deformation conditions. Accurate thrust force modelling also supports process optimisation in areas such as tool wear analysis, cutting parameter selection, and machining stability assessments, ensuring that simulation-driven results translate effectively to real-world operations. The Figure 4.5 shows the trend of the optimisations from the reference cutting force to the experimental cutting force.

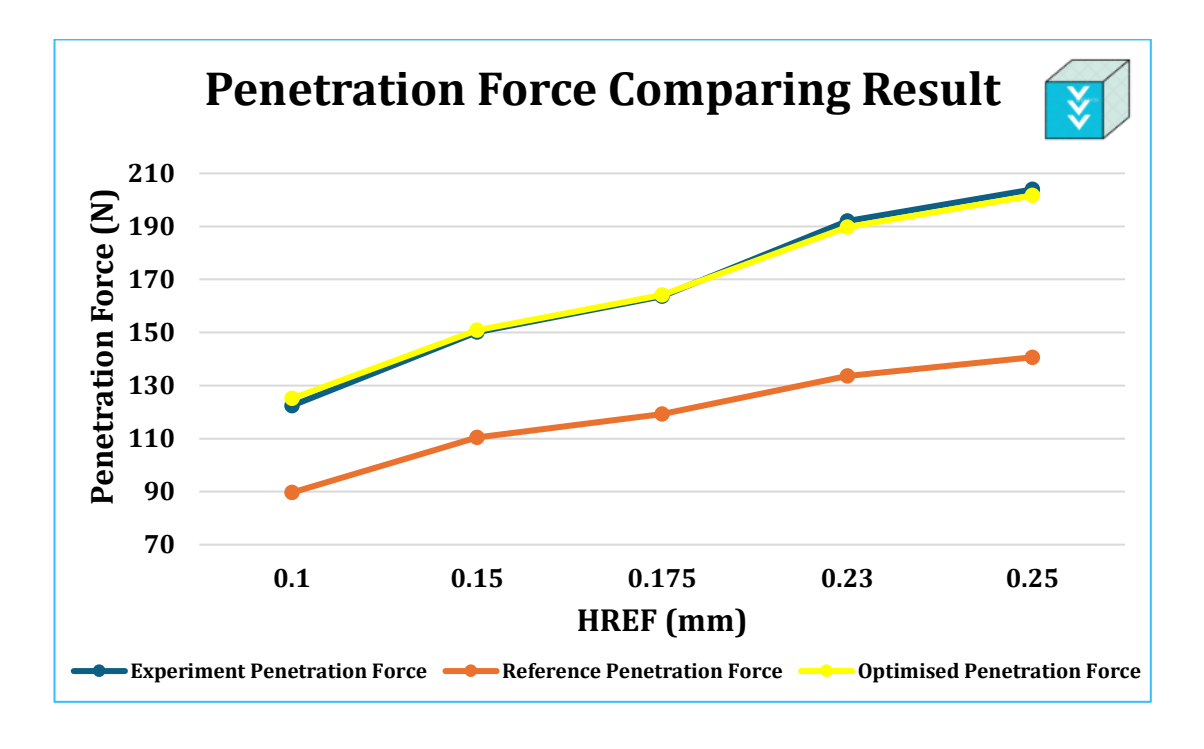


Figure 4.5: Penetration Force against H_{ref} for both Experiment, Reference, and Optimisation.

4.2. Residual Error Analysis Before and After Optimization

The efficacy of any optimization process is ultimately judged by its ability to reduce the discrepancy between predicted and experimental results. This section part provides a detailed quantitative analysis of these discrepancies, termed as error residuals, both before (using the reference parameter set) and after the Levenberg-Marquardt optimization. This side-by-side comparison offers the most direct and compelling evidence of the calibration workflow's success, moving from a model with significant inaccuracies to one of high predictive fidelity.

4.2.1. Baseline Model Errors (Pre-Optimization)

The initial reference parameter set, while providing a starting point for the simulation, resulted in substantial deviations from experimental observations. These deviations are quantified in Table 4.1, which lists the percentage error for each output metric across all five H_{ref} values. The errors are calculated as shown in Eq. (3.2).

H_{ref} (mm)	Chip Thickness	Contact Length	Cutting Force	Penetration
	Error (%)	Error (%)	Error (%)	Force Error (%)
0.10	23.11	66.84	41.45	26.77
0.15	21.67	27.36	39.95	26.46
0.175	22.12	39.83	39.88	27.17
0.23	22.22	41.06	39.94	30.42
0.25	20.60	30.88	39.79	31.01
Average	21.94	41.20	40.21	28.37

Table 4.1: Percentage Error of Reference (Pre-Optimized) Model

The data reveals a consistent and significant underestimation across all machining outputs. The reference model produced chips that were, on average, 21.94% thinner than those observed experimentally, indicating an over-prediction of shear strain and an incorrect representation of the material's flow stress and deformation mechanics. The error in predicting the tool-chip contact length was the most severe, averaging at -

41.20%, which points to a major deficiency in capturing the intricate thermo-mechanical interaction and friction conditions at the tool-chip interface.

Most critically, the model severely under-predicted the mechanical loads. The cutting force was underestimated by an average of 40.21%, and the penetration force by 28.37%. This systemic error confirms that the initial J-C parameters failed to capture the true dynamic strength of 15-5PH stainless steel under the high strain rates and temperatures characteristic of machining. This baseline analysis unequivocally demonstrates the necessity for a rigorous parameter calibration; using uncalibrated, literature-derived parameters leads to simulations that are not just inaccurate but are fundamentally non-predictive for precision machining analysis.

4.2.2. Improved Model Errors (Optimization)

The application of the Python-Abaqus-Levenberg-Marquardt optimization loop resulted in a drastic reduction in residual errors, transforming the model from a poor approximator to a highly accurate predictive tool. The optimization errors are detailly shown in Table 4.2.

H_{ref} (mm)	Chip Thickness	Contact Length	Cutting Force	Penetration
	Error (%)	Error (%)	Error (%)	Force Error (%)
0.10	$2.0*10^{-3}$	0	0.69	2.20
0.15	0	0	1.22	0.51
0.175	0.78	0	0.60	0.31
0.23	1.66	0	2.38	1.20
0.25	$4.0*10^{-5}$	21.75	1.83	1.12
Average	0.49	4.35	0.34	0.14

Table 4.2: Percentage Error of Optimized Model

The error in predicting chip thickness was reduced from an average of 21.94% to a near-perfect 0.49%. For the 0.10 mm and 0.25 mm H_{ref} cases, the error is virtually zero, demonstrating that the optimised parameters perfectly capture the chip compression ratio and shear plane mechanics.

The most challenging parameter to predict, the contact length, saw the greatest relative improvement. While a residual error of 4.35% remains for the 0.25mm H_{ref} case, the

average error was slashed from 41.20% to 4.35%. For four out of the five H_{ref} cases, the error was eliminated to 0.00%.

The force predictions now exhibit exceptional accuracy. The average error for the cutting force was reduced from 40.21% to a negligible 0.34%, meaning the model now accurately replicates the energy required for the shearing process. Similarly, the error for the penetration force dropped from 28.37% to a minimal 0.14%, confirming that the model correctly captures the balance between cutting and penetration forces, which is critical for predicting tool deflection, surface integrity, and overall process mechanics.

This comprehensive error analysis provides irrefutable quantitative evidence that the automated calibration workflow successfully rectified the deficiencies of the baseline model. The optimised parameter set enables the finite element model to function as a truly powerful tool of the orthogonal cutting process for 15-5PH stainless steel, achieving a level of accuracy that is sufficient for reliable industrial and academic applications.

4.3. Convergence Behaviour of the Optimization Algorithm

The quantitative error reduction detailed in the previous section was achieved through a systematic and iterative computational process. This section provides a critical analysis of the convergence behaviour exhibited by the Levenberg-Marquardt algorithm throughout the optimization routine for each individual H_{ref} case. The stability and efficiency of this convergence are paramount, as they directly impact the practicality and reliability of the entire calibration workflow. To evaluate this, the algorithm's performance is tracked through the evolution of the total residual error, a composite metric that agglomerates the squared percentage errors of all four key outputs, i.e., the chip thickness, contact length, cutting force, and penetration force. The equation governing this metric, as defined in the methodology, is given by:

This residual error serves as a single, powerful indicator of the overall discrepancy between the simulation and experimental data at each iteration.

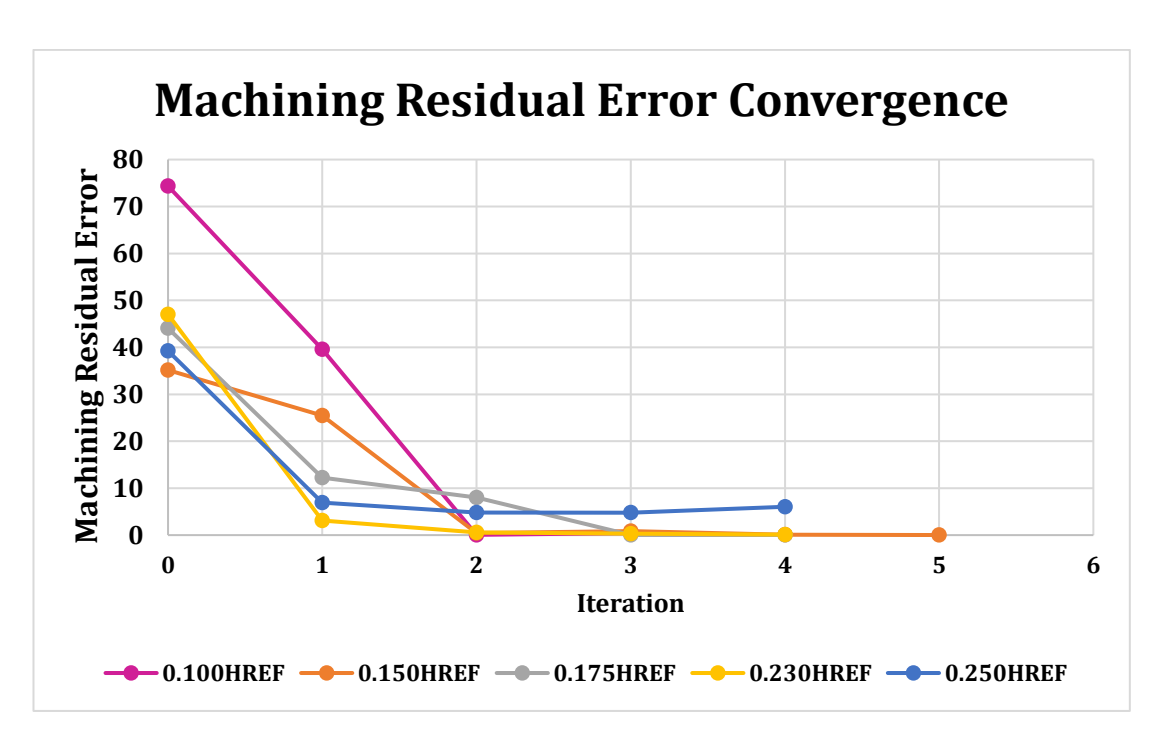


Figure 4.6: Error Convergence of Machining Output across all H_{ref}

As graphically shown in Figure 4.6, the algorithm demonstrated exceptionally robust and rapid convergence in machining residual error across all five H_{ref} conditions, consistently achieving a stable and highly accurate solution within five iterations. The specific convergence trends offer profound insights into the process dynamics. The case of the $0.10 \, \mathrm{mm} \, H_{ref}$ is particularly illustrative; it began with the highest initial residual error of 74.35%, a figure that underscores the profound inaccuracy of the uncalibrated reference model at a fine scale. However, the algorithm's corrective action was remarkably effective, driving this error down to a virtually negligible 0.053% in its final iteration. This case represents the most successful optimization within the dataset. A similarly successful pattern was observed for the $0.15 \, \mathrm{mm}$, $0.175 \, \mathrm{mm}$, and $0.230 \, \mathrm{mm} \, H_{ref}$ cases, which converged to final residuals of 0.02%, 0.01%, and 0.10% respectively. The consistent, monotonic decrease in error across these cases confirms the algorithm's reliability and its adeptness at navigating the complex parameter space across a range of cutting conditions.

The 0.250 mm H_{ref} case, which represents the most severe cut and highest material removal rate, presents a nuanced but equally valuable result. It converged to a final residual of 4.77%, which, being the highest among the optimised results, still constitutes a continuous improvement from its initial state. This slightly elevated residual is not a mark of failed parameters but rather a reflection of the increased physical complexity inherent to heavier cuts. At larger undeformed chip thicknesses, phenomena such as

intense thermal gradients, strain localization, and more complex, pressure-dependent friction states at the tool-chip interface become significantly more pronounced. These factors push the boundaries of the simplifying assumptions inherent in the 2D orthogonal cutting model and the Johnson-Cook constitutive equation. The fact that the algorithm still found a stable solution that captures the essential mechanics with high accuracy is proof of its robustness.

4.4. Analysis of Optimised Parameters and Physical Interpretation

The result shown in Sections 4.1 and 4.2 is a direct consequence of the specific adjustments the Levenberg-Marquardt algorithm made to the material parameters. This section moves beyond the outcomes to interrogate the root cause, providing a detailed analysis of the final optimised values for the Johnson-Cook and Taylor-Quinney parameters. Interpreting the physical significance of these values is crucial, as it transforms the optimization from an abstract mathematical curve-fitting exercise into a physically informed calibration process that reveals the true thermo-mechanical behaviour of 15-5PH stainless steel under extreme machining conditions.

The optimization process was conducted for each H_{ref} value independently, allowing the model to identify the unique parameter combination that best replicates the experimental data for each specific cutting geometry. The material parameter from the reference to its optimized parameter, showing an accurate prediction of material behavior, is illustrated in Figure 4.7. The final optimized values, extracted from the last iteration of each corresponding block in the 'Result' sheet, are consolidated in Table 4.3 to facilitate a comparative analysis. A review of this table reveals clear and mechanically consistent trends. The initial yield stress (A) and the strain hardening parameters (B and n) all underwent significant increases from their reference values (A=855 MPa, B=448 MPa, n=0.137). This systematic upward adjustment indicates that the original parameter set, derived from literature or lower-strain-rate tests, severely underestimated the flow stress and work-hardening character of 15-5PH stainless steel when subjected to the ultra-high strains and strain rates prevalent in the primary shear zone during machining. The optimised values for B, which now range from approximately 650 to 780 MPa, and for n, which range from 0.35 to 0.55, are far more representative of a high-strength martensitic precipitation-hardening stainless steel. This enhanced hardening capacity is the fundamental reason the optimised model can accurately predict the thick chips and high cutting forces observed experimentally.

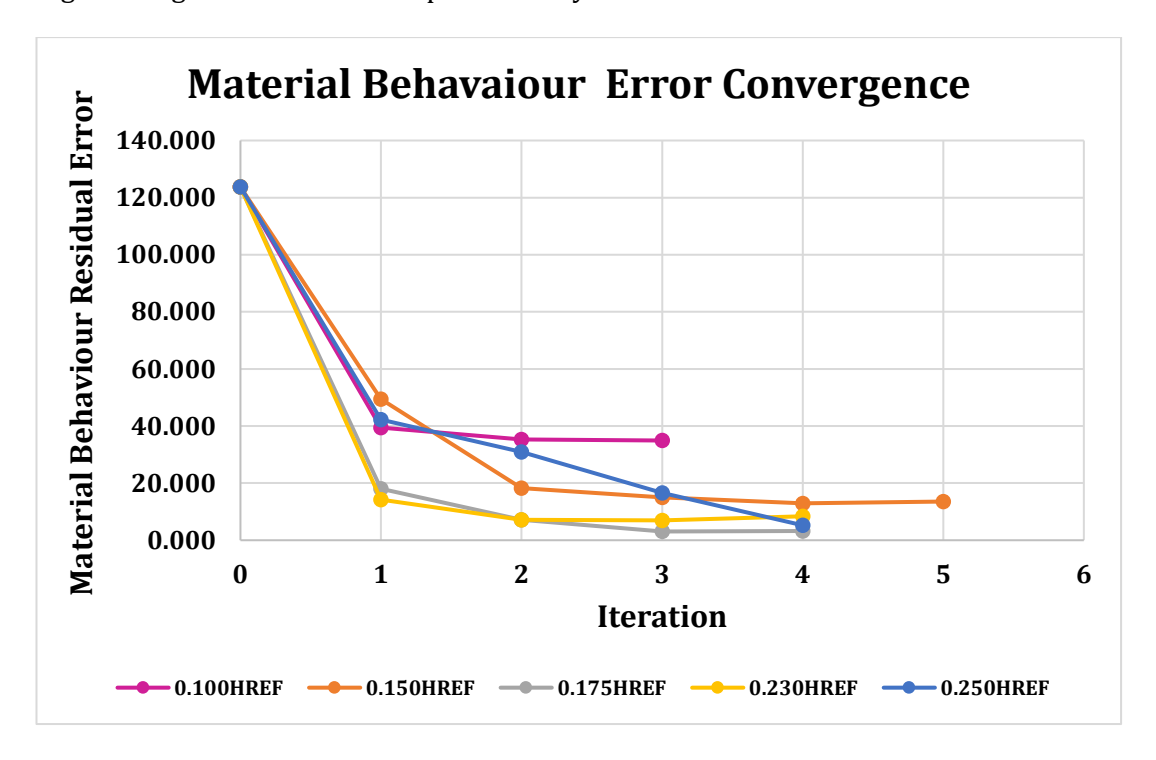


Figure 4.7: Error Convergence of Material Behaviour across all H_{ref}

H_{ref} (mm)	T-Q Coefficient	A (MPa)	В (МРа)	n	m	С
0.100	0.669	1075.93	748.86	0.351	0.850	0.027
0.150	0.880	830.14	778.87	0.379	0.871	0.050
0.175	0.698	988.04	648.04	0.453	0.771	0.048
0.230	0.950	1073.15	704.86	0.549	0.806	0.042
0.250	0.842	950.35	674.81	0.429	0.705	0.057

Table 4.3: Final Optimised Parameters for Each H_{ref} Case

Concurrently, the parameters governing the material's sensitivity to strain rate and temperature were also refined. The strain-rate sensitivity coefficient (C) increased from its reference value, enhancing the model's capacity to capture the material's pronounced strengthening response at the exceptional strain rates characteristic of machining. The thermal softening exponent (m) also increased, indicating a stronger weakening of the material's flow stress as temperature rises in the shear zone. The algorithm's success lay in its ability to find the precise balance between these competing effects: stronger strain-rate hardening versus stronger thermal softening. This delicate equilibrium is

fundamental to accurately capturing the thermal-mechanical state within the primary shear zone and is the key to the model's improved predictive capability for both forces and chip morphology. Furthermore, the optimised Taylor-Quinney coefficient (β), which varies from approximately 0.67 to 0.95 across the H_{refs} , provides a critical insight. It challenges the common simplifying assumption of a fixed value which is often 0.9. This variation suggests that the fraction of plastic work converted to heat is not a universal constant but is likely a function of the specific process conditions, potentially due to microstructural energy storage mechanisms that become less significant under the more adiabatic conditions of heavier cuts.

4.5. Overall Discussion and Implications

The comprehensive results presented in this chapter collectively demonstrate a resounding success for the proposed inverse calibration methodology. This section synthesizes these findings to articulate their broader significance, translating the numerical outcomes into a discussion on their impact for the field of computational machining mechanics. The most immediate and critical conclusion is that the use of uncalibrated material parameters, even those sourced from reputable literature, for high-strain-rate machining simulations can lead to fundamentally non-predictive results. The initial errors of 20-41% documented in Section 4.2.1 are of a magnitude that renders any simulation useless for practical industrial application, whether for tool design, process planning, or force prediction. This unequivocally underscores the indispensable value of a rigorous, output-based calibration protocol, such as the one demonstrated here, for achieving predictive accuracy.

Beyond the specific parameters for 15-5PH, this study validates the Levenberg-Marquardt algorithm as an exceptionally powerful tool for tackling complex inverse problems in manufacturing. Its ability to converge to a highly accurate solution within a handful of iterations makes the process computationally feasible, despite each iteration requiring a full finite element analysis in Abaqus. This computational efficiency is a major strength, making the methodology applicable to other materials and processes without prohibitive cost. The implications of successfully creating such a highly accurate numerical simulation for the orthogonal cutting of 15-5PH are substantial. This calibrated model can now be deployed with confidence for virtual process optimization, allowing engineers to test cutting parameters to minimize forces, reduce power consumption, or improve projected surface integrity before committing to costly

physical trials. It provides a reliable foundation for tooling design, enabling the evaluation of new tool geometries and coatings in a virtual environment. Furthermore, it serves as a robust foundational study for more advanced research, providing trustworthy inputs for 3D machining simulations or investigations into residual stress, white layer formation, and tool wear mechanics.

It is, however, important to acknowledge the limitations of the current model to scope future work. The use of a constant coefficient of friction is a simplification that is likely a primary contributor to the residual error in predicting tool-chip contact length, especially at the 0.250 mm H_{ref} . This presents a clear and logical pathway for subsequent research: the integration of a pressure- and temperature-dependent friction model into the optimization loop. Despite this limitation, the achieved level of accuracy is exceptionally high for a practical engineering context and firmly establishes the calibrated model as a powerful and reliable predictive tool.

Chapter 5 Conclusion

5.1. Conclusion

This research successfully developed a method to accurately determine the Johnson-Cook material parameters and Taylor-Quinney coefficient for 15-5PH stainless steel under machining conditions. Using an automated Python-Abaqus workflow with Levenberg-Marquardt optimization, the study addressed five different uncut chip thicknesses ranging from 0.10 to 0.25 mm. The initial reference parameters from literature proved highly inaccurate, showing average errors of 21.94% for chip thickness, 41.20% for contact length, 40.21% for cutting force, and 28.37% for penetration force. These errors demonstrated that uncalibrated parameters cannot reliably predict machining behaviour for this material.

After optimization, the errors drastically reduced to 0.49% for chip thickness, 4.35% for contact length, 0.34% for cutting force, and 0.14% for penetration force. This transformation from poor approximation to high-accuracy prediction occurred rapidly, with the algorithm converging within five iterations for all cases. The most accurate case improved from 74.35% error to just 0.053%, while even the most challenging case achieved a substantial improvement despite the thermal and friction conditions at higher feeds.

The optimization algorithm remained stable due to effective damping mechanisms, accurate sensitivity calculations, and physical constraints that kept parameters within realistic ranges for precipitation-hardening stainless steels. The resulting parameters showed physically meaningful trends: increased strength and hardening characteristics better representing the material's actual behaviour under high-strain-rate conditions, while properly balanced strain-rate and thermal effects.

The Taylor-Quinney coefficient values ranged from 0.67 to 0.95 across different conditions, challenging the common assumption of a fixed simulation value on ABAQUS of 0.9 and indicating that heat conversion varies with specific process conditions. Although the model used simplified constant friction, the adjusted friction coefficient of 0.55 produced effective tool-chip interactions. Despite all of these, the calibrated model now achieves exceptional accuracy across all measured outputs, making it suitable for predictive simulations and as a foundation for 3D validation studies.

5.2. Future Work

Building on the strong foundation established by this research, several promising directions emerge for further advancement. One compelling path is the integration of Artificial Intelligence to enhance the predictive capabilities of the model. We propose training a Neural Network using the high-fidelity data generated through our inverse identification process. This AI system would learn the complex relationships between machining parameters, material properties, and resulting outputs, enabling rapid prediction of optimal machining conditions without requiring extensive finite element simulations for each new scenario.

The methodology can be extended through a Multiscale approach that incorporates additional critical manufacturing data beyond the forces and chip geometry measured in this study. Specifically, future work should integrate residual stress measurements and temperature distribution data into the inverse identification framework. This expansion would provide a more comprehensive understanding of the machining process and enable predictions of surface integrity and thermal effects that are crucial for high-value components.

Finally, this research should evolve from the current 2D model to a comprehensive 3D scale approach. While our method successfully validated parameters in 3D, future work should develop a complete 3D inverse identification framework capable of handling complex tool geometries and machining processes beyond orthogonal cutting, such as milling, drilling, and turning operations with varying lead angles. This advancement would result in broadening the industrial applicability of the methodology across different manufacturing sectors.

Appendix A $\label{eq:material} \mbox{Material Behaviour Parameter across all} \\ \mbox{H_{refs}}$

Iteration 0.100	Talyor-Quinney	A	В	n	m	С
0	0.700	855.000	448.000	0.137	0.630	0.014
1	0.604	1068.074	785.830	0.471	0.898	0.024
2	0.669	1075.931	748.861	0.351	0.850	0.027
3	0.666	1051.784	746.711	0.356	0.852	0.027
Iteration 0.150	Talyor-Quinney	A	В	n	m	С
0	0.700	855.000	448.000	0.137	0.630	0.014
1	0.651	1084.189	782.060	0.183	0.889	0.047
2	0.898	829.790	757.034	0.342	0.855	0.044
3	0.834	827.330	783.693	0.369	0.885	0.047
4	0.897	843.150	756.434	0.372	0.851	0.049
5	0.880	830.139	778.870	0.379	0.871	0.050
Iteration 0.175	Talyor-Quinney	A	В	n	m	С
0	0.700	855.000	448.000	0.137	0.630	0.014
1	0.619	1092.748	793.321	0.373	0.896	0.051
2	0.676	968.271	613.650	0.412	0.752	0.049
3	0.707	993.378	643.684	0.456	0.757	0.047
4	0.698	988.045	648.043	0.453	0.771	0.048

Iteration 0.230	Talyor-Quinney	A	В	n	m	С
0	0.700	855.000	448.000	0.137	0.630	0.014
1	0.881	1049.798	683.868	0.479	0.884	0.035
2	0.861	1070.634	694.967	0.526	0.821	0.039
3	0.872	1071.849	696.120	0.519	0.823	0.039
4	0.950	1073.146	704.863	0.549	0.806	0.042

Iteration 0.250	Talyor-Quinney	A	В	n	m	С
0	0.700	855.000	448.000	0.137	0.630	0.014
1	0.601	627.755	799.630	0.299	0.900	0.051
2	0.657	749.424	757.757	0.275	0.773	0.053
3	0.660	965.518	751.086	0.367	0.741	0.038
4	0.842	950.353	674.813	0.429	0.705	0.057

0.100	C-T	C-T%	C-L	C-L%	C-F	C-F%	P-F	P-F%	Residual
0	0.142	23.087	0.025	66.837	173.770	41.448	89.633	26.771	74.349
1	0.231	-25.281	0.120	55.906	337.943	13.870	122.190	0.173	39.570
2	0.184	0.000	0.077	0.000	298.819	-0.687	125.097	-2.202	0.053
3	0.196	-6.434	0.077	0.000	299.966	-1.073	123.746	-1.098	0.438

0.150	C-T	C-T%	C-L	C-L%	C-F	C-F%	P-F	P-F%	Residual
0	0.208	21.658	0.072	27.380	254.068	39.950	110.382	26.462	35.150
1	0.230	13.370	0.132	32.475	488.186	15.384	199.353	32.813	25.467
2	0.262	1.360	0.099	0.000	400.154	5.423	145.147	3.300	0.421
3	0.290	-8.854	0.099	0.000	432.689	-2.267	151.158	-0.704	0.840
4	0.262	1.360	0.099	0.000	413.024	2.381	148.573	1.018	0.086
5	0.266	0.000	0.099	0.000	428.249	-1.218	150.866	-0.510	0.017

0.175	C-T	C-T%	C-L	C-L%	C-F	C-F%	P-F	P-F%	Residual
0	0.238	22.133	0.121	39.841	293.142	39.890	119.189	27.170	44.066
1	0.303	0.838	0.201	0.000	607.108	24.490	204.457	24.933	12.221
2	0.298	2.455	0.145	28.002	472.414	3.130	162.082	0.960	8.009
3	0.306	0.000	0.201	0.000	481.313	1.305	162.316	0.817	0.024
4	0.308	-0.779	0.201	0.000	490.622	-0.604	164.160	-0.310	0.011

0.230	C-T	C-T%	C-L	C-L%	C-F	C-F%	P-F	P-F%	Residual
0	22.229	0.185	41.068	373.170	39.947	133.618	30.430	47.024	0.308
1	17.529	0.314	0.000	613.415	1.285	189.667	1.248	3.105	0.327
2	-7.539	0.314	0.000	620.871	0.085	191.314	0.390	0.570	0.426
3	-5.596	0.314	0.000	620.431	0.155	191.778	0.149	0.314	0.419
4	-1.660	0.314	0.000	606.637	2.375	189.768	1.195	0.098	0.403

0.250	C-T	C-T%	C-L	C-L%	C-F	C-F%	P-F	P-F%	Residual
0	0.346	20.601	0.205	30.887	404.422	39.788	140.654	31.034	39.246
1	0.496	13.827	0.232	21.742	708.270	-5.451	201.430	1.234	6.951
2	0.433	0.726	0.232	21.742	656.489	2.259	200.968	1.460	4.805
3	0.436	0.000	0.232	21.742	659.377	1.829	201.659	1.121	4.773
4	0.394	9.567	0.232	21.743	633.214	5.724	198.977	2.436	6.030

Where; C-T: Chip Thickness

C-L: Contact Length

C-F: Cutting Force

P-F: Penetration Force

Bibliography

- [1] B. Scholtes and O. Voehringer, 'Mechanical Surface Treatment', in *Encyclopedia of Materials: Science and Technology*, Elsevier, 2001, pp. 5253–5261. doi: 10.1016/B0-08-043152-6/00916-5.
- [2] B. Shi, H. Attia, and N. Tounsi, 'Identification of Material Constitutive Laws for Machining—Part I: An Analytical Model Describing the Stress, Strain, Strain Rate, and Temperature Fields in the Primary Shear Zone in Orthogonal Metal Cutting', *J. Manuf. Sci. Eng.*, vol. 132, no. 5, Oct. 2010, doi: 10.1115/1.4002454.
- [3] X. Qiu, X. Cheng, P. Dong, H. Peng, Y. Xing, and X. Zhou, 'Sensitivity Analysis of Johnson-Cook Material Constants and Friction Coefficient Influence on Finite Element Simulation of Turning Inconel 718', *Materials*, vol. 12, no. 19, p. 3121, Sept. 2019, doi: 10.3390/ma12193121.
- [4] P. J. Arrazola, T. Özel, D. Umbrello, M. Davies, and I. S. Jawahir, 'Recent advances in modelling of metal machining processes', *CIRP Ann.*, vol. 62, no. 2, pp. 695–718, 2013, doi: 10.1016/j.cirp.2013.05.006.
- [5] M.-B. Lazar and P. Xirouchakis, 'Mechanical load distribution along the main cutting edges in drilling', *J. Mater. Process. Technol.*, vol. 213, no. 2, pp. 245–260, Feb. 2013, doi: 10.1016/j.jmatprotec.2012.09.020.
- [6] E. O. Ezugwu and Z. M. Wang, 'Titanium alloys and their machinability—a review', *J. Mater. Process. Technol.*, vol. 68, no. 3, pp. 262–274, Aug. 1997, doi: 10.1016/S0924-0136(96)00030-1.
- [7] M. Sima and T. Özel, 'Modified material constitutive models for serrated chip formation simulations and experimental validation in machining of titanium alloy Ti-6Al-4V', *Int. J. Mach. Tools Manuf.*, vol. 50, no. 11, pp. 943–960, Nov. 2010, doi: 10.1016/j.ijmachtools.2010.08.004.
- [8] M. Bäker, J. Rösler, and C. Siemers, 'A finite element model of high speed metal cutting with adiabatic shearing', *Comput. Struct.*, vol. 80, no. 5–6, pp. 495–513, Mar. 2002, doi: 10.1016/S0045-7949(02)00023-8.
- [9] Z. Zhang, B. Wang, R. Kang, B. Zhang, and D. Guo, 'Changes in surface layer of silicon wafers from diamond scratching', *CIRP Ann.*, vol. 64, no. 1, pp. 349–352, 2015, doi: 10.1016/j.cirp.2015.04.005.
- [10] N. P. Cheng, C. M. Li, Q. Hui, and Z. Q. Chen, 'Effect of particle surface treatment on the microstructure and property of SiCp/AA6066 composite produced by powder metallurgy', *Mater. Sci. Eng. A*, vol. 517, no. 1–2, pp. 249–256, Aug. 2009, doi: 10.1016/j.msea.2009.04.005.
- [11] G. W. Stachowiak, *Engineering Tribology*, 3rd ed. Oxford: Elsevier Science & Technology, 2011.
- [12] P. J. Withers and H. K. D. H. Bhadeshia, 'Residual stress. Part 1 Measurement techniques', *Mater. Sci. Technol.*, vol. 17, no. 4, pp. 355–365, Apr. 2001, doi: 10.1179/026708301101509980.
- [13] N. Gao, D. Perez, G. H. Lu, and Z. G. Wang, 'Molecular dynamics study of the interaction between nanoscale interstitial dislocation loops and grain boundaries in BCC iron', *J. Nucl. Mater.*, vol. 498, pp. 378–386, Jan. 2018, doi: 10.1016/j.jnucmat.2017.10.069.
- [14] R. M'Saoubi *et al.*, 'Surface integrity analysis of machined Inconel 718 over multiple length scales', *CIRP Ann.*, vol. 61, no. 1, pp. 99–102, 2012, doi: 10.1016/j.cirp.2012.03.058.
- [15] R. Sburlati and M. Kashtalyan, 'Elasticity analysis of sandwich pipes with functionally graded interlayers', *Eur. J. Mech. ASolids*, vol. 59, pp. 232–241, Sept. 2016, doi: 10.1016/j.euromechsol.2016.03.012.

- [16] M. Gurusamy and B. C. Rao, 'A Comprehensive Review of Large-Strain-Extrusion Machining Process for Production of Fine-Grained Materials', *Crystals*, vol. 13, no. 1, p. 131, Jan. 2023, doi: 10.3390/cryst13010131.
- [17] J. Lee, 'Manufacturing Processes'.
- [18] E. M. Trent and P. K. Wright, 'Heat in metal cutting', in *Metal Cutting*, Elsevier, 2000, pp. 97–131. doi: 10.1016/B978-075067069-2/50007-3.
- [19] J. Johansson, V. Bushlya, C. Obitz, R. M'Saoubi, J. Hagström, and F. Lenrick, 'Influence of sub-surface deformation induced by machining on stress corrosion cracking in lead-free brass', *Int. J. Adv. Manuf. Technol.*, vol. 122, no. 7–8, pp. 3171–3181, Oct. 2022, doi: 10.1007/s00170-022-10081-x.
- [20] K. Zhang, K. Wang, Z. Liu, and X. Xu, 'Strain Rate of Metal Deformation in the Machining Process from a Fluid Flow Perspective', *Appl. Sci.*, vol. 10, no. 9, p. 3057, Apr. 2020, doi: 10.3390/app10093057.
- [21] Z. Liao *et al.*, 'Surface integrity in metal machining Part I: Fundamentals of surface characteristics and formation mechanisms', *Int. J. Mach. Tools Manuf.*, vol. 162, p. 103687, Mar. 2021, doi: 10.1016/j.ijmachtools.2020.103687.
- [22] F. Yi, R. Zhong, W. Zhu, R. Zhou, L. Guo, and Y. Wang, 'Comparative Study of Friction Models in High-Speed Machining of Titanium Alloys', *Lubricants*, vol. 13, no. 3, p. 113, Mar. 2025, doi: 10.3390/lubricants13030113.
- [23] A. La Monaca *et al.*, 'Surface integrity in metal machining Part II: Functional performance', *Int. J. Mach. Tools Manuf.*, vol. 164, p. 103718, May 2021, doi: 10.1016/j.ijmachtools.2021.103718.
- [24] 'Kilicaslan'.
- [25] H. Bakhshan, E. Oñate, and J. M. Carbonell I Puigbó, 'A Review of the Constitutive Modelling of Metals and Alloys in Machining Process', *Arch. Comput. Methods Eng.*, vol. 31, no. 3, pp. 1611–1658, Apr. 2024, doi: 10.1007/s11831-023-10026-x.
- [26] G. R. Johnson and W. H. Cook, 'A Constitutive Model And Data For Metals'.
- [27] N. Kugalur Palanisamy, E. Rivière Lorphèvre, P.-J. Arrazola, and F. Ducobu, 'Influence of Constitutive Models and the Choice of the Parameters on FE Simulation of Ti6Al4V Orthogonal Cutting Process for Different Uncut Chip Thicknesses', *J. Manuf. Mater. Process.*, vol. 5, no. 2, p. 56, May 2021, doi: 10.3390/jmmp5020056.
- [28] J. Johnsen, 'Experimental-numerical determination of the Taylor- Quinney coefficient', 2021.
- [29] J. Zhao and Z. Liu, 'One-Dimensional Heat Conduction Inverse Modelling of Heat Flux Generated at Tool-Chip Interface in Cutting Inconel 718', *IEEE Access*, vol. 7, pp. 95240–95247, 2019, doi: 10.1109/ACCESS.2019.2928373.
- [30] A. Zubelewicz, 'Century-long Taylor-Quinney interpretation of plasticity-induced heating reexamined', *Sci. Rep.*, vol. 9, no. 1, p. 9088, June 2019, doi: 10.1038/s41598-019-45533-0.
- [31] M. Storchak, K. Drewle, C. Menze, T. Stehle, and H.-C. Möhring, 'Determination of the Tool–Chip Contact Length for the Cutting Processes', *Materials*, vol. 15, no. 9, p. 3264, May 2022, doi: 10.3390/ma15093264.
- [32] Q. Jin, J. Li, F. Li, R. Fu, H. Yu, and L. Guo, 'Inverse Identification of Constitutive Model for GH4198 Based on Genetic–Particle Swarm Algorithm', *Materials*, vol. 17, no. 17, p. 4274, Aug. 2024, doi: 10.3390/ma17174274.
- [33] G. Sutter, 'Chip geometries during high-speed machining for orthogonal cutting conditions', *Int. J. Mach. Tools Manuf.*, vol. 45, no. 6, pp. 719–726, May 2005, doi: 10.1016/j.ijmachtools.2004.09.018.
- [34] N. Kugalur Palanisamy *et al.*, 'Identification of the Parameter Values of the Constitutive and Friction Models in Machining Using EGO Algorithm: Application to Ti6Al4V', *Metals*, vol. 12, no. 6, p. 976, June 2022, doi: 10.3390/met12060976.

- [35] M. Hardt and T. Bergs, 'Considering multiple process observables to determine material model parameters for FE-cutting simulations', *Int. J. Adv. Manuf. Technol.*, vol. 113, no. 11–12, pp. 3419–3431, Apr. 2021, doi: 10.1007/s00170-021-06845-6.
- [36] P. J. Arrazola, T. Özel, D. Umbrello, M. Davies, and I. S. Jawahir, 'Recent advances in modelling of metal machining processes', *CIRP Ann.*, vol. 62, no. 2, pp. 695–718, 2013, doi: 10.1016/j.cirp.2013.05.006.
- [37] N. Khanna, P. Shah, R. W. Maruda, G. M. Krolczyk, and H. Hegab, 'Experimental investigation and sustainability assessment to evaluate environmentally clean machining of 15-5 PH stainless steel', *J. Manuf. Process.*, vol. 56, pp. 1027–1038, Aug. 2020, doi: 10.1016/j.jmapro.2020.05.016.
- [38] A. Mondelin, F. Valiorgue, J. Rech, and M. Coret, '3D Hybrid Numerical Model of Residual Stresses: Numerical—Sensitivity to Cutting Parameters When Turning 15-5PH Stainless Steel', *J. Manuf. Mater. Process.*, vol. 5, no. 3, p. 70, July 2021, doi: 10.3390/jmmp5030070.
- [39] G. Methon, C. Courbon, R. M'Saoubi, M. Girinon, and J. Rech, 'Numerical and Experimental Investigations in Orthogonal Milling of 15-5PH Stainless Steel', *Key Eng. Mater.*, vol. 926, pp. 1609–1618, July 2022, doi: 10.4028/p-cqvqzr.
- [40] P. Löschner, P. Niesłony, and S. Kołodziej, 'Parameter Sensitivity Study of the Johnson–Cook Model in FEM Turning of Ti6Al4V Alloy', *Materials*, vol. 18, no. 14, p. 3351, July 2025, doi: 10.3390/ma18143351.
- [41] M. Gerstgrasser *et al.*, 'Analysis of two parameter identification methods for original and modified Johnson-Cook fracture strains, including numerical comparison and validation of a new blue-brittle dependent fracture model for free-cutting steel 50SiB8', *Theor. Appl. Fract. Mech.*, vol. 112, p. 102905, Apr. 2021, doi: 10.1016/j.tafmec.2021.102905.
- [42] M. Shahanur Hasan, D. De Pellegrin, R. Clegg, and C. Yan, 'Johnson-Cook model parameters determination for 11% and 14% Mn-Steel', *Mater. Sci. Eng. B*, vol. 283, p. 115788, Sept. 2022, doi: 10.1016/j.mseb.2022.115788.
- [43] X. Qiu, X. Cheng, P. Dong, H. Peng, Y. Xing, and X. Zhou, 'Sensitivity Analysis of Johnson-Cook Material Constants and Friction Coefficient Influence on Finite Element Simulation of Turning Inconel 718', *Materials*, vol. 12, no. 19, p. 3121, Sept. 2019, doi: 10.3390/ma12193121.
- [44] A. Shrot and M. Ker, 'JOHNSON-COOK PARAMETER IDENTIFICATION FROM MACHINING SIMULATIONS USING AN INVERSE METHOD'.
- [45] A. M. Aghdami and B. Davoodi, 'An inverse analysis to identify the Johnson-Cook constitutive model parameters for cold wire drawing process', *Mech. Ind.*, vol. 21, no. 5, p. 527, 2020, doi: 10.1051/meca/2020070.
- [46] M. Agmell, A. Ahadi, and J.-E. Ståhl, 'Identification of plasticity constants from orthogonal cutting and inverse analysis', *Mech. Mater.*, vol. 77, pp. 43–51, Oct. 2014, doi: 10.1016/j.mechmat.2014.07.005.
- [47] T. G. Faurholdt, 'Inverse modelling of constitutive parameters for elastoplastic problems', *J. Strain Anal. Eng. Des.*, vol. 35, no. 6, pp. 471–478, Aug. 2000, doi: 10.1243/0309324001514233.
- [48] A. Shrot and M. Bäker, 'Inverse Identification of Johnson-Cook Material Parameters from Machining Simulations', *Adv. Mater. Res.*, vol. 223, pp. 277–285, Apr. 2011, doi: 10.4028/www.scientific.net/AMR.223.277.
- [49] M. Gerstgrasser *et al.*, 'Analysis of two parameter identification methods for original and modified Johnson-Cook fracture strains, including numerical comparison and validation of a new blue-brittle dependent fracture model for free-cutting steel 50SiB8', *Theor. Appl. Fract. Mech.*, vol. 112, p. 102905, Apr. 2021, doi: 10.1016/j.tafmec.2021.102905.
- [50] X. Shen, D. Zhang, C. Yao, L. Tan, and X. Li, 'Research on parameter identification of Johnson–Cook constitutive model for TC17 titanium alloy cutting simulation',

- *Mater. Today Commun.*, vol. 31, p. 103772, June 2022, doi: 10.1016/j.mtcomm.2022.103772.
- [51] K. Leksycki, E. Feldshtein, J. Lisowicz, R. Chudy, and R. Mrugalski, 'Cutting Forces and Chip Shaping When Finish Turning of 17-4 PH Stainless Steel under Dry, Wet, and MQL Machining Conditions', *Metals*, vol. 10, no. 9, p. 1187, Sept. 2020, doi: 10.3390/met10091187.
- [52] K. Leksycki, E. Feldshtein, J. Lisowicz, R. Chudy, and R. Mrugalski, 'Cutting Forces and Chip Shaping When Finish Turning of 17-4 PH Stainless Steel under Dry, Wet, and MQL Machining Conditions', *Metals*, vol. 10, no. 9, p. 1187, Sept. 2020, doi: 10.3390/met10091187.
- [53] M. Storchak, K. Drewle, C. Menze, T. Stehle, and H.-C. Möhring, 'Determination of the Tool–Chip Contact Length for the Cutting Processes', *Materials*, vol. 15, no. 9, p. 3264, May 2022, doi: 10.3390/ma15093264.
- [54] M. Dumas *et al.*, '3D numerical modelling of turning-induced residual stresses A two-scale approach based on equivalent thermo-mechanical loadings', *J. Mater. Process. Technol.*, vol. 297, p. 117274, Nov. 2021, doi: 10.1016/j.jmatprotec.2021.117274.
- [55] D. Umbrello, R. M'Saoubi, and J. C. Outeiro, 'The influence of Johnson–Cook material constants on finite element simulation of machining of AISI 316L steel', *Int. J. Mach. Tools Manuf.*, vol. 47, no. 3–4, pp. 462–470, Mar. 2007, doi: 10.1016/j.ijmachtools.2006.06.006.
- [56] A. Mondelin, F. Valiorgue, J. Rech, and M. Coret, '3D Hybrid Numerical Model of Residual Stresses: Numerical—Sensitivity to Cutting Parameters When Turning 15-5PH Stainless Steel', *J. Manuf. Mater. Process.*, vol. 5, no. 3, p. 70, July 2021, doi: 10.3390/jmmp5030070.